2006

Exchange Coupling Mediated Through-Bonds and Through- Space in Conformationally-Constrained Polyradical Scaffolds: Calix[4]arene Nitroxide Tetraradicals And Diradical

Andrzej Rajca
University of Nebraska - Lincoln, arajca1@unl.edu

Sumit Mukherjee
University of Nebraska-Lincoln

Maren Pink
Indiana University

Suchada Rajca
University of Nebraska-Lincoln, srajca1@unl.edu

Published in final edited form as:
J Am Chem Soc. 2006 October 18; 128(41): 13497–13507. doi:10.1021/ja063567+.

Exchange Coupling Mediated Through-Bonds and Through-Space in Conformationally-Constrained Polyradical Scaffolds: Calix[4]arene Nitroxide Tetraradicals And Diradical

Andrzej Rajca[*,a], **Sumit Mukherjee**[a], **Maren Pink**[b], and **Suchada Rajca**[a]

a*Department of Chemistry, University of Nebraska, Lincoln, NE 68588-0304. IUMSC*

b*Department of Chemistry, Indiana University, Bloomington, IN 47405-7102*

Abstract

Calix[4]arenes constrained to 1,3-alternate conformation and functionalized at the upper rim with four and two *tert*-butylnitroxides have been synthesized, and characterized by X-ray crystallography, magnetic resonance (EPR and ^{1}H NMR) spectroscopy, and magnetic studies. The 1,3-alternate nitroxide tetraradical and diradical provide unique polyradical scaffolds for dissection of the through-bond and through-space intramolecular exchange couplings. In addition, detailed magnetic studies of the previously reported calix[4]arene nitroxide tetraradical, which possesses cone conformation in solution, reveal conformational dependence of exchange coupling. Through-bond coupling between the adjacent nitroxide radicals is mediated by the nitroxide-*m*-phenylene-CH_2-*m*-phenylene-nitroxide coupling pathway, and through-space coupling is found between the diagonal nitroxide radicals at the conformationally-constrained N···N distance of 5–6 Å. Magnetic studies of the calix[4]arene polyradical scaffolds in frozen solutions show that the through-bond exchange coupling in the 1,3-alternate calix[4]arene tetraradical is antiferromagnetic, while that in cone calix[4]arene tetraradical is ferromagnetic. The through-space exchange couplings are antiferromagnetic in both cone and 1,3-alternate calix[4]arene tetraradical, as well as in the 1,3-alternate calix[4]arene diradical. The exchange coupling constants ($|J/k|$) are of the order of 1 Kelvin.

Introduction

The spin-spin interactions between unpaired electrons in organic diradicals and polyradicals are of critical importance in organic magnetism,[1-3] molecular charge-transfer,[4] and multiple spin labeling in structural biology.[5] When unpaired electrons are in close proximity, the dominant interaction is likely to be exchange coupling, mediated through bonds and/or through space.[1] In general, the exchange coupling is mediated more effectively through bonds, especially through cross-conjugated π-system, than through space.[3,6-10] Such exchange coupling can be either ferromagnetic or antiferromagnetic, depending upon the topology and conformation of the coupling pathway connecting the radicals.[1,8-12]

Stable polyradical scaffolds with constrained conformations may provide a new approach for controlling through-bond and through-space exchange couplings. The fixed conformations of 1,3-alternate and cone calix[4]arenes, that are functionalized at the upper rim with stable aryl-delocalized radicals, may be viewed as such scaffolds.[13a,14] In these scaffolds, the through-

* To whom correspondence should be addressed. E-mail: arajca1@unl.edu.

Supporting Information Available: general procedures and materials, additional experimental details (synthesis of **4**, SQUID magnetometry data, EPR spectra), and X-ray crystallographic files in CIF format. This material is available free of charge via the Internet at http://pubs.acs.org.

bond exchange coupling between the adjacent radicals is mediated by the radical-*m*-phenylene-CH_2-*m*-phenylene-radical coupling pathway, with distinct conformations in the 1,3-alternate and cone calix[4]arenes (Figure 1). In addition, the through-space exchange coupling at fixed radical-radical distances of approximately 5–6 Å, as found for the diagonal radicals, may be probed (Figure 1).

Recently, we reported synthesis, crystallography, and magnetic characterization of the cone calix[4]arene scaffold, nitroxide tetraradical **3** (Figure 2).[13] In the solid state, this tetraradical adopts a pinched cone conformation, forming an intramolecular dimer with strong antiferromagnetic coupling ($|J/k|$ = 200–300 K) between the two diagonal nitroxides. In solution, **3** was found to possess a 4-fold symmetric cone conformation but exchange coupling could only be estimated as 30 K > $|J/k| \gg$ 1.8 mK.[13] Now we report the synthesis and studies of ambient stable nitroxide tetraradical **1** and diradical **2** in the fixed 1,3-alternate calix[4]arene conformations (Figure 2). Magnetic studies of **1** and **2**, as well as magnetic studies of **3** in solution, are described. Both through-bond and through-space exchange couplings are determined, as well as their conformational dependence.

Results and Discussion

Synthesis

The synthesis starts from tetrabromocalix[4]arene **4**, constrained in the 1,3-alternate conformation (Scheme 1 and Supporting Information).[15] The Li/Br exchange on **4** with an excess amount of *t*-BuLi gives intermediate tetrakis(aryllithium), which is reacted with 2-methyl-2-nitrosopropane dimer, to provide tetrahydroxylamine **5**. An analogous procedure, in which the *t*-BuLi is replaced with *n*-BuLi (2 equiv),[16] gives dihydroxylamine **6**.

The presence of the hydroxyl groups in **5** and **6** is confirmed by IR (e.g., $\nu_{O\text{-}H} \approx$ 3230–3240 cm^{-1}) and ^1H NMR spectra (D_2O-exchangable 4-proton or 2-proton singlet at 9.1–9.3 ppm). In the ^1H NMR spectra, only one sharp singlet for *tert*-butyl group protons is observed for each compound. The other ^1H resonances are relatively broadened at ambient temperature, due to the restricted rotations along the C(aromatic)-N bonds; the coalescence temperatures for aromatic protons suggest that the barrier for rotation is on the order of 15 kcal mol^{-1} (Table S1, Supporting Information). In the high temperature limit, **5** and **6** possess D_{2d} (T > 325 K) and C_{2v} (T > 306 K) point groups, respectively, on the ^1H NMR (400 MHz) time scale.

Oxidation of **5** and **6** with freshly prepared silver oxide give the corresponding nitroxide tetraradical **1** and diradical **2** (Scheme 1).

Molecular structure of 1 and 2

Nitroxide tetraradical **1** crystallizes with one molecule per asymmetric unit, without inclusion of solvent. For diradical **2**, two crystallographically unique molecules are found, with one quarter benzene molecule per formula unit (one half benzene molecule per asymmetric unit). The X-ray structure determinations of nitroxide tetraradical **1** and diradical **2** confirm 1,3-alternate conformation of the calix[4]arene macrocycle for both molecules (Figure 3, Table 1).

In tetraradical **1**, the molecular structure is consistent with significant repulsion between the bulky *tert*-butyl nitroxide moieties. The N-C(*ipso*)-C(*para*) angles of <180° (e.g., N1-C3-C6 angle of 172°) and pyramidalized nitrogen atoms indicate outward bending of the nitroxide groups, with relatively long N1···N3 (5.78 Å) and N2···N4 (5.70 Å) distances between the diagonal nitroxide groups. Dihedral angles between nitroxide groups and benzene rings are significantly different for each of the four aryl nitroxide units; for each pair of the diagonal *tert*-butyl nitroxide moieties, the bulky *tert*-butyls occupy the significant part of the space between the nitroxide groups (Figure 4).

In diradical **2**, the structures for the two crystallographically unique molecules show the two nitroxide groups in relatively closer proximity, with N···N distances 5.07 and 5.37 Å and nearly planar nitrogen atoms, compared to **1**. In one of the unique molecules, the NO groups have antiparallel N-O bond axes (*anti*) and they are coplanar with the benzene rings within each aryl nitroxide moiety. In the other molecule, the NO groups have parallel N-O bond axes (*syn*) and they form torsional angles of ~40° with the benzene rings within each aryl nitroxide moiety.

For **1** and **2**, the C(*ipso*)-C(CH_2)-C(*ipso*) angles within calix[4]arene macrocycles are in the 110 – 113° range.[17] The dihedral angles between the planes defined by the C(*ipso*)-C(CH_2)-C(*ipso*) and the benzene rings are in the 59–73° range (Table S2, Supporting Information). In this geometry of 1,3-alternate conformation, the π-systems of the adjacent arylnitroxides are pointing away from each other. However, in a cone conformation, which is adopted by tetraradical **3** in solution, the dihedral angles between the C(*ipso*)-C(CH_2)-C(*ipso*) and benzene ring planes are close to 90°, with the π-systems of the adjacent arylnitroxides pointing toward each other. Therefore, the through-space interactions between the adjacent arylnitroxide moieties in the 1,3-alternate conformation of **1** should be relatively small, compared to those in the cone conformation of **3**.

Structure of 1 and 2 in solution

^{1}H NMR spectra of tetraradical **1** and diradical **2** in chloroform-*d* at room temperature show resonances for those protons that are expected to possess relatively small spin densities, i.e., all protons except those of the aryl moieties of the arylnitroxides (Figure 5).[1b,13a,18,19]

Four broad resonances are observed for tetraradical **1**, as expected for a structure with the D_{2d} point group. The relatively less broadened 12-proton and 16-proton singlets at 4.34 and 3.84 ppm are assigned to the methyl (CH_3) and dimethylene (CH_2CH_2) of the methoxyethyleneoxy ($OCH_2CH_2OCH_3$) groups, respectively. The two most up-field shifted broad singlets, 8-proton at −0.8 ppm and 36-proton at −5.9 ppm, are assigned to the methylene groups of the macrocycle and the *tert*-butyl groups, respectively.

Four broad resonances with similar chemical shifts to those in **1** may be identified for diradical **2**; specifically, two of those resonances appear in the −5 ppm region as a broad singlet with a shoulder, which may be assigned to the two *tert*-butyl groups and four methylene groups of the macrocycle.[20] In addition, relatively narrow singlets at 7.47, 4.30, and 3.69 ppm are assigned to the aromatic, OCH_3, and OCH_2CH_2O protons of the diamagnetic bromophenyl moieties of **2**, respectively.

The significant up-field chemical shifts of several parts-per-million for the protons of *tert*-butyl groups and of methylene groups in tetraradical **1** and diradical **2**, when compared to the corresponding hydroxylamines **5** and **6**, indicate substantial negative spin densities at the hydrogen atoms in these groups. The negative sign of the spin density for the hydrogen atoms of the *tert*-butyl groups is consistent with the spin polarization through σ-bonds of the positive spin density at the nitrogen atom of the nitroxide, as found for *N*-*tert*-butylnitroxides.[21] The negative sign for the hydrogen atoms of the methylene groups is compatible with both hyperconjugation and spin polarization of the negative spin density from the *meta*-carbon (*meta*-position with respect to the nitroxide) in the benzene ring.[22] The near coincidence of resonances for the methyl (CH_3) and dimethylene (CH_2CH_2) of the methoxyethyleneoxy ($OCH_2CH_2OCH_3$) groups in **1** and **2**, and in diamagnetic **5** and **6**, suggests negligible spin densities at the hydrogen atoms of OCH_2 fragment. Similar behavior was found in 3,5-dimethyl-4-methoxyphenyl-*tert*-butylnitroxide, in which a very small value of ^{1}H-hyperfine splitting, a_H = +0.0006 mT, for the methoxy hydrogens was ascribed to the twisting of the methoxy group out of conjugation with the benzene ring and the nitroxide.[22,23] These ^{1}H

NMR spectral assignments confirm the structures of **1** and **2** in solution, and are in agreement with the reported spectra for the fixed cone calix[4]arene nitroxide tetraradical **3**.[13a]

EPR spectrum of **1** in toluene at 295 K shows a well-resolved nonet (Figure 6). An excellent numerical spectrum fit to a single component, i.e., nitroxide tetraradical **1**, is obtained, confirming high degree of radical purity (98+ %) of **1**.[24] The ^{14}N hyperfine coupling with peak-to-peak splitting $\Delta H_{pp} \approx 0.319$ mT = $a_N/4$, i.e., $a_N = 1.28$ mT, is identical to the value reported for 3,5-dimethyl-4-methoxyphenyl-*tert*-butylnitroxide.[22,25] This result indicates exchange-coupled nitroxides with a coupling constant significantly greater than the ^{14}N hyperfine coupling, $|J/g\mu_B| \gg |a_N|$, i.e., $|J/k| \gg 1.8$ mK. At 135 K, the EPR spectrum of **1** in toluene glass shows a single peak in the $|\Delta m_s| = 1$ region, with a somewhat broader spectral envelope, compared to the solution phase spectrum for the same sample (Figure 6). Furthermore, the $|\Delta m_s| = 2$ transition is barely detectable. These results suggest that tetraradical **1** possesses rather small zero-field splitting ($|D/hc|$) that is compatible with relatively high average symmetry for the disposition of nitroxide radicals.[26,27]

EPR spectra of diradical **2** in solution (toluene, toluene/chloroform (4:1), acetonitrile, dichloromethane, and dichloromethane/methanol (4:1)) at ambient temperature show an intense broad peak, with discernable pentuplet spectral pattern; furthermore, additional sharp peaks, with relatively low intensity, are superimposed on the broad peak (Figure S6–S9, Supporting Information). The EPR spectra of **2** in dichloromethane/methanol (4:1) show pronounced sharpening at higher temperatures, with a clearly defined pentuplet at 320 K; upon decreasing the temperature, this peak is progressively broadened. For 1 mM solution of **2** in toluene at 295 K, the numerical spectrum fits are compatible with a mixture of diradical and monoradical (98:2). Because of the dynamic effects, the quality of these fits is rather low, especially compared to those for tetraradical **1**;[28] consequently, the ^{14}N hyperfine coupling with peak-to-peak splitting $\Delta H_{pp} \approx 0.8$ mT = $a_N/2$, i.e., $a_N = 1.6$ mT for **2**, should be viewed as an approximate estimate. These results are in agreement with significant exchange coupling between nitroxide radicals ($|J/g\mu_B| \gg |a_N|$).

In rigid matrices, the EPR spectra of **2** clearly show the presence of significant zero-field splitting, as indicated by the large spectral width of $|\Delta m_s| = 1$ region and relatively intense $|\Delta m_s| = 2$ transition. The $|\Delta m_s| = 1$ spectrum of **2** in toluene/chloroform glass at 140 K consists of four symmetrically disposed broad peaks, corresponding to the zero-field splitting parameters $|D/hc| = 1.39\times10^{-2}$ cm^{-1} and $|E/hc| = 0$ cm^{-1}(Figure 7). Similar four-peak $|\Delta m_s| = 1$ spectra are obtained at low temperatures in 2-methyltetrahydrofuran, dichloromethane/methanol (4 : 1), and ethanol (Figures S10 and S11, Supporting Information); for the first two matrices, the two side peaks consist of five symmetrically disposed shoulders (pentuplet-like), corresponding to the ^{14}N hyperfine coupling with spacings of $(|A_{zz}|/2)/hc \approx 0.0013$ cm^{-1} ($(|A_{zz}|/2)/g\mu_B \approx 1.4$ mT). (The pentuplet in the $|\Delta m_s| = 2$ region possesses similar 1.4-mT line spacings.) It is usually assumed that the largest principal values of the magnetic dipole tensor and nuclear hyperfine tensor correspond to the direction of the *z*-axis connecting the nitroxide radicals and the direction of the nitrogen $2p_\pi$-orbital, respectively.[29] The observation of the relatively large value of $|A_{zz}|/2$ in the $|\Delta m_s| = 1$ region suggests that these two directions are approximately coinciding; this may correspond to the limiting conformation of diradical **2**, with the parallel N-O bond axes and the planar phenylnitroxide moieties. Spectral widths of the $|\Delta m_s| = 1$ regions, $|2D/g\mu_B| = 29 – 31$ mT, are solvent dependent. Based upon a simple point-dipole approximation, $|2D/g\mu_B| = 29 – 31$ mT corresponds to an effective distance of about 5.6 – 5.8 Å between the two magnetic dipoles.[30] For 1 mM **2** in toluene/chloroform (4 : 1) with $|2D/g\mu_B| = 30$ mT, the relative intensities of the $|\Delta m_s| = 1$ and $|\Delta m_s| = 2$ transitions are 5.06×10^{-4} at 9.4848 GHz, providing the interspin distance estimate of 5.73 Å.[31] These distance measurements, which are comparable to the expected distance between the mid-points of the N-O bonds of the diagonal nitroxides in the 1,3-alternate conformation of **2**, should be

viewed as approximate estimates, as the spin density in **2** is delocalized and factors other than magnetic dipole-dipole interactions may contribute to the value of $|2D|$.

The EPR spectra support structural assignments for **1** and **2**, and provide the lower bound estimate for $|J|$, similar to that found for **3**. Values of J are determined by magnetic studies of **1** – **3**.

Magnetic studies of 1, 2, and 3 in solution

Magnetization (M) is measured as a function of magnetic field (H = 0–5×10^4 Oe and T = 1.8, 3, and 5 K) and temperature (T = 1.8–300 K at H = 30000, 5000, or 500 Oe). The M vs. H and M vs. T data are plotted as the M/M_{sat} vs. H/T and the χT vs. T, respectively, where M_{sat} is the magnetization at saturation and χ is the paramagnetic susceptibility.

For tetraradical **1** in tetrahydrofuran (THF), the value of χT is constant in the 40–150 K range (Figure 8). The downward turn in the χT vs. T plot at low temperature is consistent with antiferromagnetic exchange coupling, corresponding to a mean-field parameter, $\theta \approx -2.3$ K. The antiferromagnetic exchange coupling is most likely intramolecular, as the curvature and onset of the downward turn is not dependent on concentration of **1** (5 and 13 mM). The presence of antiferromagnetic exchange coupling is also indicated by the relatively slow saturation behavior for the M vs. H data; the M/M_{sat} vs. H/T plots at T = 1.8–5 K have significantly different curvatures, that are much smaller than the curvature of the Brillouin curve for four independent spins S = ½.

Considering their structural similarity, magnetic studies of diradical **2** may provide additional insight into the nature of intramolecular antiferromagnetic exchange coupling in tetraradical **1**. For 7 mM **2** in THF (Figure 9), the relatively small curvature of the downward turn in the χT vs. T plot at low temperature and the slightly different curvatures of the M/M_{sat} vs. H/T plots in the T = 1.8–5 K range are readily corrected with a small mean-field parameter $\theta \approx -0.5$ K, accounting for weak antiferromagnetic exchange coupling between two spins S = ½. Similar weak antiferromagnetic coupling ($\theta \approx -0.5$ K) is observed for more concentrated, 15 and 24 mM, samples of **2** in THF (Figure S13 and S14, Supporting Information).

Magnetic data for 5 mM **1** in 2-MeTHF and ~5 mM **2** in chloroform/methanol (1:1) suggest significantly weaker antiferromagnetic exchange couplings, $\theta = -1.5$ K and $\theta = -0.1$ – (-0.2) K, respectively; for **2**, the magnetic data are approaching the near perfect paramagnetic behavior of two independent spins S = ½ (Figure S16, Supporting Information).

These results indicate that exchange coupling in diradical **2** in THF is intramolecular and it is significantly weaker, compared to that in tetraradical **1** in THF. This suggests that the stronger antiferromagnetic exchange coupling in tetraradical **1** is mediated through bonds, with the coupling pathway consisting of nitroxide-*m*-phenylene-CH_2-*m*-phenylene-nitroxide; in diradical **2**, with the additional *m*-phenylene-CH_2 unit in the coupling pathway, the through-bond exchange coupling should be negligible.[32] This would imply that the weak antiferromagnetic exchange coupling for **2** in THF may be associated with the through-space exchange coupling between the diagonal nitroxides. Such through-space exchange coupling is likely to be antiferromagnetic and strongly dependent on the distance between the nitroxides (NO). Although the N···N distance in the 1,3-alternate conformation of **2** is fixed at 5–6 Å, rotation along the C(aryl)-N bonds may provide conformations with significantly different N···O and O···O distances that may lead to modulation of the through-space exchange coupling between the diagonal nitroxides. The evidence for such conformations is obtained from X-ray crystallography and EPR spectroscopy of **2**. In particular, the nitroxide-nitroxide distances, as measured by the values of $|2D|$ for **2**, and the strength of the through-space antiferromagnetic exchange coupling are dependent on the solvent (matrix).

For tetraradical **1** and diradical **2**, both temperature-dependence (χT vs. T) and field-dependence (M vs. H) of the experimental magnetic data are well fit by the tetraradical model and the diradical model, respectively. In these models, based upon the Heisenberg Hamiltonian ($2JS_n \bullet S_{n+1}$),[33] tetraradical **1** may be viewed as a cluster of four S = ½ spins located at the vertices of a square (Figure 10, eq. 1 and 2); analogously, diradical **2** may be considered as a dimer of two diagonally positioned S = ½ spins (Figure 10, eq. 3 and 4). Each of the four identical pairwise exchange couplings (J_1/k), along the sides of the square, corresponds primarily to the through-bond exchange coupling between the adjacent nitroxides, mediated by the nitroxide-*m*-phenylene-CH_2-*m*-phenylene-nitroxide coupling pathway in **1**. Each of the two diagonal exchange couplings (J_2/k) in the square corresponds to the through-space exchange coupling between the diagonal nitroxides in **1** and **2**. Another variable parameter is used to account for impurities and inaccuracies in the mass balance, i.e., "magnetization at saturation," M_{sat} (eq. 1 and 3, expressed in units of Bohr magnetons per nitroxide) and the mass factor, w (eq. 2 and 4). (For selected fits, the mean-field parameter, θ, could be used in place of J_2/k.) N denotes number of moles of tetraradical (eq. 1 and 3). Equations 1 – 4 account for paramagnetic saturation.

$$M=(11180N)M_{sat}[\,2(F_1+F_2)/(G_1+G_2)] \quad (1)$$

$$\chi T=(1.118T/H)w[\,2(F_1+F_2)/(G_1+G_2)] \quad (2)$$

$$M=(11180N)M_{sat}[\,(F_1+F_2)/(G_1+G_2)] \quad (3)$$

$$\chi T=(1.118T/H)w[\,(F_1+F_2)/(G_1+G_2)] \quad (4)$$

$$F_1=\sinh(a)+2\sinh(2a)$$

$$F_2=[\,\sinh(a)][\,(\exp((-4J_1/k)/T))+2(\exp((-(2J_1+2J_2)/k)/T))]$$

$$G_1=1+2\cosh(a)+2\cosh(2a)+(\exp((-6J_1/k)/T)+(\exp((-(2J_1+4J_2)/k)/T))$$

$$G_2=[\,1+2\cosh(a)][\,(\exp((-4J_1/k)/T))+2(\exp((-(2J_1+2J_2)/k)/T))]$$

$$a=1.345[\,H/(T-\theta)]$$

The two-parameter numerical fits of the χT vs. T and the M/M_{sat} vs. H/T data for diradical **2** in THF, using the diradical model (eq. 3 and 4, with J_1/k set to zero), give $J_2/k \approx -0.7$ K for the through-space exchange coupling between the diagonal nitroxides (Figure 9, and Figure S15, Supporting Information).[34]

The numerical fits of **1** to the tetraradical model (Figure 10) would require three variable parameters: J_1/k,J_2/k, and w (or M_{sat}). Because such three-parameter fits are typically overparametrized, the fits with two variable parameters for the χT vs. T data are considered. The two-parameter fits for tetraradical **1** in THF, which account only for the through-space exchange coupling (J_2/k) as in diradical **2**, give $J_2/k \approx -2$ K and unsatisfactory coefficient of determination (R^2 = 0.96, eq. S2, Supporting Information). The quality of two-parameter fits is improved (R^2 = 0.98) when the through-bond exchange coupling parameter is optimized ($J_1/k \approx -1.5$ K), with J_2/k set to zero; however, R^2 significantly improves, when J_2/k is set to a small negative value rather than zero. For the χT vs. T data, the best fits (R^2 = 0.998) give $J_1/k \approx -1.3$ K with J_2/k set to about −1 K. Analogous fits are obtained for the M/M_{sat} vs. H/T data, with the smaller values of $|J_1/k|$ and $|J_2/k|$ (Figure 8 and Figure S12, Supporting Information).[35] Therefore, it is concluded that the through-bond exchange couplings between the adjacent nitroxides and the through-space exchange couplings between the diagonal

nitroxides in the 1,3-alternate calix[4]arene conformation of tetraradical **1** in THF are both antiferromagnetic, with $J_1/k \approx J_2/k \approx -1$ K. Similar through-bond antiferromagnetic exchange couplings, $J_1/k \approx -0.9$ K, but weaker through-space antiferromagnetic exchange couplings, $J_2/k \approx -0.3$ K, are obtained for 5 mM **1** in 2-MeTHF.[36]

The results of magnetic studies for ~20 mM tetraradical **3** in THF or 2-MeTHF (Figure 11 and Figure S18, and S19, Supporting Information) are qualitatively different, compared to those for **1** in THF or 2-MeTHF. Notably, the χT vs. T plot for **3** shows an upward turn at $T < 40$ K, consistent with the presence of ferromagnetic exchange coupling, most likely intramolecular. The ferromagnetic exchange coupling is also indicated by the relatively fast saturation behavior for the M vs. H data. The M/M_{sat} vs. H/T plots at $T = 1.8$–5 K are bracketed by the Brillouin curves corresponding to $S = 1$ and $S = 1/2$, i.e., the curvatures of the experimental data are significantly greater, compared to the theoretically predicted paramagnetic behavior for four independent spins $S = 1/2$. In addition to this ferromagnetic exchange coupling, a weaker antiferromagnetic exchange coupling appears to be present; e.g., for 15 mM **3** in THF, an additional downward turn may be observed in the χT vs. T plot at $T \approx 2$–3 K. The strength of antiferromagnetic exchange coupling in **3** is similar to that in diradical **2**, and may be of a similar origin, i.e., due to the direct through-space exchange coupling between the diagonal nitroxides. In such a case, the magnetic data for **3** may be modeled by the cluster of four $S = ½$ spins positioned at the vertices of a square, as for tetraradical **1** (Figure 10).

The χT vs. T data for **3** in 2-MeTHF (Figure 11) provide an excellent 3-parameter fit to the tetraradical model (eq. 2), to give $J_1/k = +1.0$ K (ferromagnetic) for the through-bond exchange coupling between the adjacent nitroxides and $J_2/k = -0.7$ K (antiferromagnetic) for the direct through-space coupling between the diagonal nitroxides. An alternative numerical fit with $J_1/k = +1.3$ K is obtained, when the presence of the antiferromagnetic exchange coupling is modeled with a mean-field parameter $\theta = -0.7$ K (Figure S17, Supporting Information). Similar numerical fits are obtained for **3** in THF, though the values of $|J_2/k|$ are relatively greater (Figure S18 and S19, Supporting Information).[37,38]

Magnetic studies of 1 and 2 in the solid state

The χT vs. T plots for solid tetraradical **1** (Figure 12) and diradical **2** (Figure S20, Supporting Information) are flat, except for a downward turn at low temperatures.

In the flat sections of the plots (20–300 K), the values of $\chi T = 1.45$ and $\chi T = 0.70$ emu K mol^{-1} are measured for solid **1** and **2**, respectively. These values are in excellent agreement with the theoretical, spin-only $\chi T = 1.50$ and $\chi T = 0.75$ emu K mol^{-1} for tetraradicals and diradicals, with independent $S = ½$ radicals. Similarly, quantitative values of $\chi T \approx 1.3$–1.5 and $\chi T \approx 0.8$ emu K mol^{-1} are obtained for **1** and **2** in chloroform at room temperature (295–300 K), respectively, using the ^{1}H NMR-based Evans method.[39] Within accuracy of the Evans method, these values are in good agreement with the values of χT for solid **1** and **2**.

The downward turns of the χT vs. T plots at low temperature are consistent with overall antiferromagnetic exchange couplings between nitroxide radicals. The presence of anitferromagnetic exchange coupling is also indicated by the relatively slow saturation behavior for the M vs. H data at 1.8 K. In particular, the overall antiferromagnetic exchange coupling in **1** is significantly weaker in the solid state ($\theta \approx -0.7$ K), compared to that in THF solution ($\theta \approx -2.3$ K).

For a quantitative fit to the magnetic data for solid **1** and **2**, both intramolecular and intermolecular exchange coupling would need to be considered. Such models may be suggested by the analysis of the crystal packing.

Crystal packing of 1 and 2

Crystal packing of both **1** and **2** may be described in terms of layers of calix[4]arene macrocycles in the approximate *bc*- or (100)-plane (Figure 13, Figures S1–S3, Supporting Information).

For tetraradical **1**, dimers of nitroxides, in which the two N2-O4 moieties form two short sides of parallelogram (N2-O4-N2-O4 torsion of 180°), with intermolecular O4···O4 distance of 4.60 Å, are found. Another intermolecular distance is the O1···N1 distance of 4.75 Å, which is found in a uniform one-dimensional zig-zag chain of nitroxides along the c-axis (N1-O1-N1-O1 torsion of 166 °). In addition, short intermolecular O···C distances (O1···C2 = 3.97 Å and O4···C11 = 3.58 Å) between the nitroxide groups and the corresponding *ortho*-carbon atoms of the benzene rings are found. For each O···C distance, the N-O bond axis and the $2p_{\pi}$(C)-orbital axis (centered on carbon atom) are nearly orthogonal, with the N-O bond axis pointing approximately toward the nodal plane of the $2p_{\pi}$(C)-orbital. As these intermolecular interactions are associated with relatively long distances and may contribute to either ferromagnetic or antiferromagnetic exchange coupling, their overall impact on magnetic data of solid **1** is probably small but not negligible. The χT vs. T and the M/M_{sat} vs. H/T data for solid **1** may still be fit to the tetraradical model (Figure 10, equations 1 and 2) but the antiferromagnetic exchange coupling $J_1/k \approx -0.6$ K is much smaller compared to that in the analogous fits of the solution data with J_2/k set to zero. However, in contrast to the samples of **1** in THF, the numerical fits for solid **1** could not be improved by the additional weak antiferromagnetic exchange couplings, such as $J_2/k < 0$ or $\theta < 0$, reflecting the impact of crystal packing on magnetic data.

For diradical **2**, the shortest intermolecular contacts are associated with the rectangular dimers of nitroxides, which are formed between the two crystallographically unique molecules; the N2A···O6B and N2B···O6A distances of 4.96 and 4.98 Å are found, respectively (Figure S3, Supporting Information). Therefore, for one half of the nitroxide radicals, pairwise intermolecular antiferromagnetic exchange coupling in solid **2** is expected. This intermolecular exchange coupling may be described by the "diradical plus two monoradicals" model. In this model, the one half of the nitroxide radicals, forming dimers, corresponds to exchange-coupled "diradicals" and the other half of the nitroxide radicals are treated as independent $S = ½$ "monoradicals". A comparable numerical fit for solid **2** is obtained using the diradical model, describing intramolecular exchange coupling only.

For **1** and **2**, the magnetic data in the solid state, in conjunction with the analysis of crystals packing, are consistent with the magnetic data in solution. Nevertheless, the magnetic data for **1** and **2** in frozen solutions, devoid of detectable intermolecular exchange coupling, are far more informative.

Conformational dependence of exchange coupling in 1 – 3

The magnetic studies of **1**, **2**, and **3** in frozen THF (or 2-MeTHF) indicated that the through-bond exchange coupling between the adjacent nitroxides, mediated by the nitroxide-*m*-phenylene-CH_2-*m*-phenylene-nitroxide coupling pathway, is antiferromagnetic in **1** ($J_1/k \approx -1$ K) and ferromagnetic in **3** ($J_1/k \approx +1$ K). In addition, the through-space exchange coupling between the diagonal nitroxides in **1**, **2**, and **3** is antiferromagnetic ($J_2/k \approx -1$ K).

For cross-conjugated *m*-phenylene-based diradicals, exchange coupling changes from ferromagnetic ($J > 0$) to antiferromagnetic ($J < 0$) when the radical moieties are twisted out of the plane of the *m*-phenylene with torsional angles of near 90 °.[40-43] For diradicals, in which radical moieties are cross-conjugated through two *m*-phenylenes, i.e., through 3,3'-biphenylyne, antiferromagnetic exchange couplings are typically found;[32b,44,45] however,

there is no clear-cut evidence for the change of sign of *J*, upon severe twisting to the near 90 ° torsional angle along the C1-C1' bond.[9,46] For trimethylene diradicals (and the related tetraradicals) with constrained CCC-angles, Dougherty and coworkers developed the model explaining the preference for high-spin ground states (ferromagnetic exchange coupling).[7,8,47-50]

The antiferromagnetic and ferromagnetic through-bond exchange couplings in tetraradicals **1** and **3** indicate profound effect of torsions within the exchange pathway comprising of two *m*-phenylene groups and one methylene group. Although this magnetic behavior is not well understood, the relative orientations of π-systems, especially those of $2p_\pi$-orbitals of the *ipso*-carbon atoms adjacent to the methylene group, are likely to play an important role. Based upon the experimental EPR spectra and the spin polarization mechanism within the π-system, the two carbon atoms, which correspond to the non-bonding MO nodal positions of the benzylic-like radicals, are expected to possess a substantial negative π-spin density.[1,51] This electronic structure may be compared to simple diradicals such as 2,2'-bis(allyl)methane or trimethylene,[52] though their detailed analyses concerning correlations between the torsional angles and the exchange coupling are not available.[53,54] We propose the following analysis. In the 1,3-alternate calix[4]arene scaffold, the π-systems of the adjacent radicals are pointing away from each other, and in the cone, they are pointing toward each other. The relative orientations of the $2p_\pi$-orbitals at *ipso*-positions in the 1,3-alternate and the cone calix[4]arene scaffolds are analogous to the approximate (70,70)- and (90,90)-conformations of bis(allyl)methane diradical (or trimethylene diradical), derived by the conrotatory and disrotatory motion from the (0,0)-conformation, respectively (Figure 14). We suggest that the closer balance between the through-space and through-bond interactions between the adjacent radicals is attained in the cone calix[4]arene scaffold, compared to its 1,3-alternate analogue. Therefore, the cone and 1,3-alternate calix[4]arene scaffolds favor through-bond ferromagnetic and antiferromagnetic exchange coupling, respectively.

Conclusion

Through-bond and through-space exchange coupling in the calix[4]arene scaffolds functionalized on the upper rim with nitroxide radicals were studied. The through-bond exchange coupling between the adjacent nitroxide radicals is controlled by the conformation of the nitroxide-*m*-phenylene-CH_2-*m*-phenylene-nitroxide coupling pathway. In the 1,3-alternate calix[4]arene scaffold (tetraradical **1**), the exchange coupling is antiferromagnetic ($J_1/k \approx -1$ K) and, in the cone calix[4]arene scaffold (tetraradical **3**), the exchange coupling is ferromagnetic ($J_1/k \approx +1$ K). The through-space exchange coupling between the diagonal nitroxides at the N···N distance of 5–6 Å in the 1,3-alternate and cone calix[4]arene scaffolds (**1**, **2**, and **3**) is antiferromagnetic ($J_2/k < 0$), with the matrix-dependent coupling strength ($|J_2/k| < -1$ K).

Highly symmetric (D_{2d} point group) and electron-rich 1,3-alternate calix[4]arene may serve as a scaffold for polyradicals with negligible net magnetic dipole-dipole coupling and, possibly, ionophoric properties. Control of both exchange coupling and magnetic dipole-dipole coupling, as well as their modulation by metal ions, are of importance for electronic relaxation processes, especially for the development of organic paramagnetic contrast agents.[6]

Experimental Section

Tetrahydroxylamine 5

t-BuLi in pentane (1.70 M, 0.80 mL, 1.31 mmol) was added to a solution of tetrabromocalix[4]arene **4** (0.152 g, 0.156 mmol) in THF (10 mL) at −78 °C. The resultant yellowish-orange solution was stirred at −78 °C for 2 h, and then allowed to attain −25 °C for 15 min. The color

of the solution changed to a dark orange. Subsequently, the reaction mixture was cooled to −78 °C, and then a solution of 2-methyl-2-nitrosopropane dimer (65.4 mg, 0.375 mmol) in THF (3.5 mL) was added. The reaction mixture was allowed to attain room temperature overnight. The usual aqueous workup with ether, including drying over $MgSO_4$, was followed by column chromatography (TLC grade silica, 14 – 20% ether in hexanes), to yield tetrahydroxylamine **5** (75.8 mg, 48%) as a white powder. From two other reactions done on 400-mg scale, 0.205 g (49%) and 0.248 g (60%) of tetrahydroxylamine **5** was obtained from 0.402 g and 0.401 g of tetrabromocalix[4]arene **4**, respectively. M.p. 232–234 °C (under Ar, dec). ^{1}H NMR (400 MHz, $CDCl_3$): 9.277 (s, 4H, exch D_2O), 7.369 (bs, 4H, Ar*H*), 6.677 (bs, 4H, Ar*H*), 3.911 (bs, s, 12H), 3.75 (bs, 4H), 3.540 (s, 12H, OMe), 3.47, 3.36 (bs 2H), bs, 8H), 1.152 (s, 36H, *t*-Bu). ^{13}C NMR (100 MHz, $CDCl_3$): 152.6, 142.1, 132.5, 131.8, 126.2, 124.7, 124.6, 72.4, 72.2, 59.7, 59.0, 26.1. IR (ZnSe, cm^{-1}): 3225, 3090, 2931, 2875, 1592, 1454, 1386, 1359, 1210, 1125, 1063, 1030, 878. LR/HR FABMS (3-NBA matrix): *m/z* (ion type, % RA for *m/z* 500–1300, deviation for the formula) at 1005.6134 ($[M + H]^+$, 100, 3.0 ppm for $^{12}C_{56}{}^1H_{85}{}^{14}N_4{}^{16}O_{12}$), 1004.6084 ($[M]^+$, 88, 0.2 ppm for $^{12}C_{56}{}^1H_{84}{}^{14}N_4{}^{16}O_{12}$).

Dihydroxylamine 6

n-BuLi in hexane (2.14 M, 0.16 mL, 0.34 mmol) was added to a solution of tetrabromocalix [4]arene **4** (0.151 g, 0.155 mmol) in THF (10 mL) at −78 °C. The resultant bright orange solution was stirred at −78 °C for 2 h, and then allowed to attain −30 °C for 15 min. Subsequently, a dark orange solution was cooled to −78 °C, and then a solution of 2-methyl-2-nitrosopropane dimer (32.4 mg, 0.186 mmol) in THF (3 mL) was added. The reaction mixture was allowed to attain room temperature overnight. The green reaction mixture was subjected to a usual aqueous workup with ether, including drying over $MgSO_4$, and then evaporated to dryness. Column chromatography (TLC grade silica, 14 – 17% ether in hexanes) gave dihydroxylamine **6** (57.6 mg, 37%) as white powder. M.p. 218–219 °C (under N_2, dec). From another reaction on 400-mg scale, 0.183 g (44%) of dihydroxylamine **6** was obtained from 0.406 g of tetrabromocalix[4]arene **4**. ^{1}H NMR (400 MHz, $CDCl_3$): 9.124 (s, 2H, exch D_2O), 7.36 (bs, 2H), 7.260 (s, under the solvent peak, 4H), 6.79 (bs, 2H), 3.90, 3.87 (bm, m, 12H), 3.81 (m, 4H), 3.644 (s, 6H), 3.530 (s, 6H), 3.33–3.48 (bm, 8H), 1.177 (s, 18H). ^{13}C NMR (125 MHz, $CDCl_3$): 154.4, 152.6, 142.3, 135.5, 134.6, 133.2, 131.9, 114.9, 72.5, 72.4, 72.3, 72.0, 59.9, 59.4, 59.3, 58.9, 34.1, and 26.1. IR (ZnSe, cm^{-1}): 3235, 3070, 2933, 2877, 1596, 1573, 1451, 1361, 1199, 1125, 1059, 1028, 850, 717. LR/HR FABMS (3-NBA matrix): *m/z* (ion type, % RA for *m/z* 700–1500, deviation for the formula) at 991.2975 ($[M+4]^+$, 38, −7.0 ppm for $^{12}C_{48}{}^1H_{64}{}^{14}N_2{}^{16}O_{10}{}^{81}Br_2$), 988.2939 ($[M+2]^+$, 53, −3.3 ppm for $^{12}C_{48}{}^1H_{64}{}^{14}N_2{}^{16}O_{10}{}^{81}Br{}^{79}Br$), 986.2918 ($[M]^+$, 25, 1.0 ppm for $^{12}C_{48}{}^1H_{64}{}^{14}N_2{}^{16}O_{10}{}^{79}Br_2$), 970.3 ($[M-18]^+$, 100).

Nitroxide tetraradical 1

Freshly prepared silver oxide (0.285 g, 1.23 mmol) was added to a solution of tetrahydroxylamine **5** (0.124 g, 0.0199 mmol) in $CHCl_3$ (6 mL). After stirring at room temperature in darkness for 9 h, the reaction mixture was filtered, and then the red filtrate was evaporated to dryness to obtain the nitroxide tetraradical **1** (0.119 g, 96 %) as a brick-red solid. Similar procedure, except for the increased amount of silver oxide (40 vs. 15 equiv), gave 0.193 g (96%) of **1** from 0.200 g of tetrahydroxylamine **5**; this was the primary sample for magnetic and spectroscopic studies. Two other reactions were carried out with tetrahydroxylamine **5** (75.8 mg and 0.205 g) and silver oxide (40 equiv) in dichloromethane; the crudes obtained after filtration and drying, were further recrystallized from methanol, to yield 39.6 mg (52%) and 0.109 g (53%) of **1**, respectively. ^{1}H NMR spectra of the recrystallized samples showed a sharp singlet at ~3.6 ppm (1.5H, assigned to residual methanol) and a broad singlet at 7.1 ppm (0.14H). All yields are reported after correcting for the extraneous ^{1}H NMR resonances (solvent of crystallization, stopcock grease, etc.). M.p. 169–171 °C (under Ar, dec). ^{1}H NMR (500

MHz, $CDCl_3$): 4.341 (bs, 12H), 3.842 (bs, 16H), −0.753 (bs, 8H), −5.881 (v. bs, 36H). IR (ZnSe, cm^{-1}): 3078, 2978, 2930, 2878, 1576, 1458, 1347, 1203, 1123, 1050, 883. Evans method (4 measurements, $CDCl_3/CHCl_3$, 297–300 K), χT = 1.30–1.52 emu K mol^{-1} (3.6, 4.1, 4.0, 3.5 unpaired electrons).

Nitroxide diradical 2

Freshly prepared silver oxide (0.530 g, 2.286 mmol) was added to a solution of dihydroxylamine **6** (56.5 mg, 0.057 mmol) in CH_2Cl_2 (1.5 mL). After stirring at room temperature in darkness for 4 h, the reaction mixture was filtered, and then the red filtrate was evaporated to dryness to obtain a reddish-orange oil. Column purification with deactivated flash silica gel at 0 °C under nitrogen, followed by recrystallization from ether/heptane mixture gave diradical **2** (23.9 mg, 42%) as dark-red needles. From another reaction on 150-mg scale (using 20 equiv of silver oxide), 70.5 mg (47%) of diradical **2** was obtained from 0.150 g of dihydroxylamine **6**. Yields are corrected for the residual solvents (ether and heptane) remaining after recrystallization. Magnetic and spectroscopic studies were carried using another sample of **2** (orange-red solid), which was prepared from dihydroxylamine **6** and silver oxide in chloroform. M.p. 151–153 °C (under Ar, dec). ^1H NMR (500 MHz, $CDCl_3$): 7.469 (s, 4H), 4.304, 4.084, ~3.9, 3.688 (s, bs, bs, s, 28–32H), −5.132 (v. bs(sh) 22–26H). IR (ZnSe, cm^{-1}): 3077, 2929, 2875, 1574, 1451, 1364, 1195, 1124, 1054, 925, 858. Evans method (2 measurements, $CDCl_3/CHCl_3$, 298 and 300 K), $\chi T \approx 0.80, 0.78$ emu K mol^{-1} (2.2, 2.1 unpaired electrons).

Acknowledgements

This research was supported by the National Science Foundation (CHE-0107241 and CHE-0414936), including the purchase of the Electron Paramagnetic Resonance (EPR) spectrometer (DMR-0216788). Part of this research was performed in facilities renovated with support from NIH (RR16544-01). We thank Drs. Kouichi Shiraishi and Hongxian Han, and Kausik Das, for help with the EPR spectroscopy and preparation of samples for SQUID magnetometry.

References

1. (a) Iwamura H, Koga N. Acc Chem Res 1993;26:346–351. (b) Rajca A. Chem Rev 1994;94:871–893.Lahti, PM., editor. Magnetic Properties of Organic Materials. Marcel Dekker; New York: 1999. p. 1-713.Itoh, K.; Kinoshita, M., editors. Molecular Magnetism. Gordon and Breach; Kodansha: 2000. p. 1-337. (e) Rajca A. Chem Eur J 2002;8:4834–4841. (f) Rajca A. Adv Phys Org Chem 2005;40:153–199.
2. (a) Rajca A, Wongsriratanakul J, Rajca S. Science 2001;294:1503–1505. [PubMed: 11711668] (b) Rajca S, Rajca A, Wongsriratanakul J, Butler P, Choi S. J Am Chem Soc 2004;126:6972–6986. [PubMed: 15174867] (c) Rajca A, Wongsriratanakul J, Rajca S. J Am Chem Soc 2004;126:6608–6626. [PubMed: 15161289] (d) Rajca A, Wongsriratanakul J, Rajca S, Cerny RL. Chem Eur J 2004;10:3144–3157. (e) Rajca A, Shiraishi K, Vale M, Han H, Rajca S. J Am Chem Soc 2005;127:9014–9020. [PubMed: 15969578]
3. Fukuzaki E, Nishide H. J Am Chem Soc 2006;128:996–1001. [PubMed: 16417391]
4. (a) Weiss EA, Ahrens MJ, Sinks LE, Gusev AV, Ratner MA, Wasielewski MR. J Am Chem Soc 2004;126:5577–5584. [PubMed: 15113229] (b) Weiss EA, Wasielewski MR, Ratner MA. J Chem Phys 2005;123:064504–1–8. (c) Weiss EA, Tauber MJ, Kelley RF, Ahrens MJ, Ratner MA, Wasielewski MR. J Am Chem Soc 2005;127:11842–11850. [PubMed: 16104763] (d) Chernick ET, Mi Q, Kelley RF, Weiss EA, Jones BA, Marks TJ, Ratner MA, Wasielewski MR. J Am Chem Soc 2006;128:4356–4364. [PubMed: 16569012]
5. (a) Hustedt EJ, Beth AH. Ann Rev Biophys Biomol Struct 1999;28:129–153. [PubMed: 10410798] (b) Eaton SS, Eaton GR. Biol Magn Reson 2000;19:1–27. (c) Altenbach C, Oh K-J, Trabanino R, Hideg K, Hubbell W. Biochemistry 2001;40:15471–15482. [PubMed: 11747422] (d) Hanson P, Millhauser G, Formaggio F, Crisma M, Toniolo C. J Am Chem Soc 1996;118:7618–7625.

6. Spagnol G, Shiraishi K, Rajca S, Rajca A. Chem Comm 2005:5047–5049. [PubMed: 16220166]
7. Dougherty DA. Acc Chem Res 1991;24:88–94.
8. (a) Jacobs SJ, Shultz DA, Jain R, Novak J, Dougherty DA. J Am Chem Soc 1993;115:1744–1753. (b) Jacobs SJ, Dougherty DA. Angew Chem Int Ed 1994;33:1104–1106.
9. Borden WT, Iwamura H, Berson JA. Acc Chem Res 1994;27:109–116.
10. (a) Michon P, Rassat A. J Am Chem Soc 1975;97:696–700. (b) Metzner EK, Libertini LJ, Calvin M. J Am Chem Soc 1977;99:4500–4502. (c) Frank NL, Clérac R, Sutter J-P, Daro N, Kahn O, Coulon C, Green MT, Golhen S, Ouahab L. J Am Chem Soc 2000;122:2053–2061.
11. Shultz DA, Fico RM Jr, Bodnar SH, Kumar K, Vostrikova KE, Kampf JW, Boyle PD. J Am Chem Soc 2003;125:11761–11771. [PubMed: 13129381]
12. For an effect of heteroatoms on through-bond exchange coupling: (a) West AP Jr, Silvermann SK, Dougherty DA. J Am Chem Soc 1997;119:1452–1463. (b) Matsuda K, Yamagata T, Seta T, Iwamura H, Hori K. J Am Chem Soc 1997;119:8058–8064. (c) Berson JA. Acc Chem Res 1997;30:238–244. (d) Shultz DA, Bodnar SH, Lee H, Kampf JW, Incarvito CD, Rheingold AL. J Am Chem Soc 2002;124:10054–10061. [PubMed: 12188669]
13. Rajca A, Pink M, Rojsajjakul T, Lu K, Wang H, Rajca S. J Am Chem Soc 2003;125:8534–8538. [PubMed: 12848560] (b) Because of technical difficulties in measurements of magnetic susceptibility data for **3** in solution at low temperatures, wide range of values for the exchange coupling were obtained (30 K > $|J/k| \gg$ 1.8 mK).
14. Nitroxides and nitronyl nitroxides on the upper and lower rim of calix[4]arene: (a) Ulrich G, Turek P, Ziessel R. Tetrahedron Lett 1996;37:8755–8758. (b) Wang Q, Li Y, Wu G. Chem Commun 2002:1268–1269. (c) Kröck L, Shivanyuk A, Goodin DB, Rebek J Jr. Chem Commun 2004:272–273.
15. Verboom W, Datta S, Reinhoudt DN. J Org Chem 1992;57:5394–5398.
16. Larsen M, Jørgensen M. J Org Chem 1996;61:6651–6655. [PubMed: 11667536]
17. C(CH_2) and C(*ipso*) refer to the CC-bonded carbon atoms of the methylene group and benzene ring of the calix[4]arene scaffold. An example of the C(*ipso*)-C(CH_2)-C(*ipso*) angle is C5-C7-C8 angle of 112.6° in **1**.
18. La Mar, GN.; Horrocks, WDeW, Jr; Holm, RH., editors. NMR of Paramagnetic Molecules. Academic; New York: 1973.
19. Sharp RR. Nucl Magn Reson 2005;34:553–596.
20. Two types of protons (AB or AX spin system) are expected for the methylene groups of the macrocycle in diradical **2**. An AB spin system is observed for the corresponding protons in dihydroxylamine **6** at $T > 306$ K.
21. (a) Rassat A, Ray P. Tetrahedron 1973;29:2845–2848. (b) Rajca A, Lu K, Rajca S, Ross CR II. Chem Commun 1999:1249–1250.
22. Forrester AR, Hepburn SP, McConnachie G. J Chem Soc Perkin Trans I 1974:2213–2219.
23. Hyperfine splitting of a_H = +0.019 mT for the methoxy hydrogens in 4-methoxyphenyl-*tert*-butylnitroxide has been reported (ref 22).
24. The numerical fits with three components, tetraradical, triradical, and diradical, indicate 98+ % content of tetraradical. The three-component fit and the one-component fit have coincident values of hyperfine splittings for tetraradical and nearly identical sums of squared residuals (Figure S4, Supporting Information).
25. The agreement for the ^{1}H hyperfine, which is not resolved in EPR spectrum of **1**, is less satisfactory: a_H = 0.019 mT vs. 0.024 mT in **1** and in 3,5-dimethyl-4-methoxyphenyl-*tert*-butylnitroxide, respectively.
26. Wertz, JE.; Bolton, JR. Electron Spin Resonance. Chapter 10. Chapman and Hall; New York: 1986. p. 223-257.
27. The small zero-field splitting in tetraradical **1** is in contrast to the spectral width of about 20 mT in tetraradical **3** in the cone conformation in solution (ref 13).
28. Polimeno A, Zerbetto M, Franco L, Maggini M, Corvaja C. J Am Chem Soc 2006;128:4734–4741. [PubMed: 16594710]

29. Griffith OH, Cornell DW, McConnell HM. J Chem Phys 1965;43:2909–2910. (b) In particular, A_{zz} = 3.2 mT was measured in di-*tert*-butylnitroxide radical. As the solution-phase ^{14}N hyperfine splittings for aryl-alkyl nitroxide radicals, compared to the more localized alkyl-alkyl nitroxide radicals, are lowered by a typical factor of 0.8 – 0.9, the value of $|A_{zz}| \approx 2.6$ mT measured for aryl-alkyl nitroxide diradical **2** is reasonable.
30. (a) The following equation applies to distance, r (in Å), between two point-dipoles: $r = (55600/|(2D/g\mu_B)|)^{1/3}$, where $|2D/g\mu_B|$ and r are expressed in Gauss and Å, respectively. (b) For localized nitroxide diradical, in which the intramolecular distances between the midpoints of the N-O bonds were approximately 6.2 Å, $|2D/g\mu_B| \approx 25$ mT was measured: Rohde O, Van SP, Kester WR, Griffith OH. J Am Chem Soc 1974;96:5311–5318.
31. Eaton SS, More KM, Sawant BM, Eaton GR. J Am Chem Soc 1983;105:6560–6567.
32. (a) The presence of parallel exchange coupling pathways in diradical **2** may partially offset the decrease of the through-bond exchange coupling in **2**, compared to tetraradical **1**. Rajca A, Rajca S, Wongsriratanakul J. Chem Commun 2000:1021–1022.
33. Belorizky E, Fries PH. J Chim Phys (Paris) 1993;90:1077–1100.
34. The singlet ground state for diradical **2** with $J_2/k = -0.7$ K (the singlet-triplet gap of about 1 – 2 K) is consistent with the observation of thermally populated triplet state at 140 K in the EPR spectra of **2**, as well as with the lower bound of exchange coupling, $|J/g\mu_B| \gg |a_N|$, determined by the EPR spectroscopy.
35. Another model, which may be viewed as corresponding to a structure of tetraradical 1 with two distinct conformations of the diagonal pairs of nitroxides, was considered. One pair of the diagonal nitroxides was treated as a diradical with exchange coupling J_2 (Figure 10) and the other pair was treated as two independent spins $S = ½$ (eq. S6a, Supporting Information). For two-parameter numerical fits of the χT vs. T data at 5000 Oe in the warming mode for 5 mM **1** (identical sample to that in Figure 8), the variable parameters (parameter dependence and R^2) are as follows: $J_2/k = -5.2$ K, $w = 1.09$ (0.38, 0.993). For analogous three-parameter fits, in which exchange couplings for both pairs of the diagonal nitroxides are optimized, similar results are obtained, i.e., one relatively large and one several times smaller value of $|J/k|$ are found (eq. S4a with $J_1 \neq J_2$, (Supporting Information). For such distinct conformations of the diagonal pairs of nitroxides, the structure of **1** would be significantly distorted from the D_{2d} point group. However, the EPR spectra for 5 mM **1** in THF (identical sample to that in Figure 8, after magnetic measurements) show a single peak with the peak-to-peak width of 0.8 mT (8 G); thus, symmetry lowering is not detectable by EPR spectroscopy.
36. For 5 mM tetraradical **1** in 2-MeTHF, three-parameter fit has still acceptable values of parameter dependence of significantly less than one, e.g., values of parameter dependence are 0.87, 0.82, and 0.53 for J_1/k, J_2/k, and w, respectively ($R^2 = 0.998$).
37. The M/M_{sat} vs. H/T data for **3** could not be fit to the tetraradical model with ferromagnetic $J_1/k > 0$, due to overparametrization.
38. The values of $|J_1/k|$ for through-bond ferromagnetic exchange coupling between the adjacent nitroxides in tetraradical **3** may be somewhat underestimated by the present model, due to the possible contribution from antiferromagnetic exchange coupling between the adjacent nitroxides. Such through-space contribution is possible, as the adjacent nitroxides are relatively close in space in **3** with cone conformation. We thank the reviewer for pointing out the possibility of significant antiferromagnetic through-space interactions between the adjacent nitroxides in the cone conformation.
39. (a) Evans DF. J Chem Soc 1959:2003–2005. (b) Live DH, Chan SI. Anal Chem 1970;42:791–792.
40. Dvolaitzky M, Chiarelli R, Rassat A. Angew Chem Int Ed Engl 1992;31:180–181.
41. Fang S, Lee M-S, Hrovat DA, Borden WA. J Am Chem Soc 1995;117:6727–6731.
42. Rajca A, Rajca S. J Chem Soc Perkin Trans 2 1998:1077–1082.
43. A “Karplus-Conroy-type” relationship for exchange coupling in trimethylenemethane-based bis (semiquinone) diradicals was proposed: ref [11].
44. Rajca A, Rajca S. J Am Chem Soc 1996;118:8121–8126.
45. Sakane A, Kumada H, Karasawa S, Koga N, Iwamura H. Inorg Chem 2000;39:2891–2896. [PubMed: 11232829]
46. Rajca A, Utamapanya S, Smithhisler DJ. J Org Chem 1993;5:5650–5652.

47. Goldberg AH, Dougherty DA. J Am Chem Soc 1983;105:284–290.

48. (a) Hoffmann R. Acc Chem Res 1970;4:1–6. (b) Hay PJ, Thibeault JC, Hoffmann R. J Am Chem Soc 1975;97:4884–4899.

49. (a) Buchwalter SL, Closs GL. J Am Chem Soc 1975;97:3857–3858. (b) Buchwalter SL, Closs GL. J Am Chem Soc 1979;101:4688–4694.

50. Sherrill CD, Seidl ET, Schaefer HF III. J Phys Chem 1992;96:3712–3716.

51. Hyperfine splitting of a_H = 0.09 mT and a_H = 0.18 mT for the *meta* and *ortho* hydrogens in 4-methoxyphenyl-*tert*-butylnitroxide in carbon tetrachloride has been reported (ref 22). As the positive sign of a_H for the *meta* hydrogen was determined by ^{1}H NMR spectroscopy, this implies the presence of negative π-spin density at the *meta* carbon.

52. We thank the reviewer for pointing out that bis(allyl)methane diradical would be a better model, compared to trimethylene diradical.

53. 2,2'-Bis(allyl)methane diradical was apparently generated as an intermediate upon thermolysis of 1,3-dimethylenecyclopentane: (a) Gajewski JJ, Salazar JDC. J Am Chem Soc 1981;103:4145–4154. (b) Gajewski JJ, Salazar JDC. J Am Chem Soc 1981;103:4145–4154.

54. Calculations on trimethylene diradical: (a) Yamaguchi Y, Osamura Y, Schaefer HF III. J Am Chem Soc 1983;105:7506–7511. (b) Skancke A, Hrovat DA, Borden WT. J Am Chem Soc 1998;120:7079–7084.

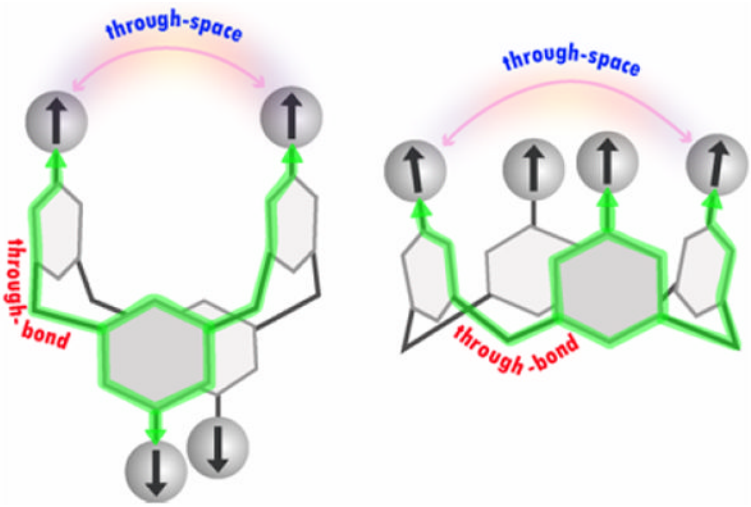

Figure 1.
1,3-Alternate and cone calix[4]arene scaffolds, functionalized on the upper rims with radicals.

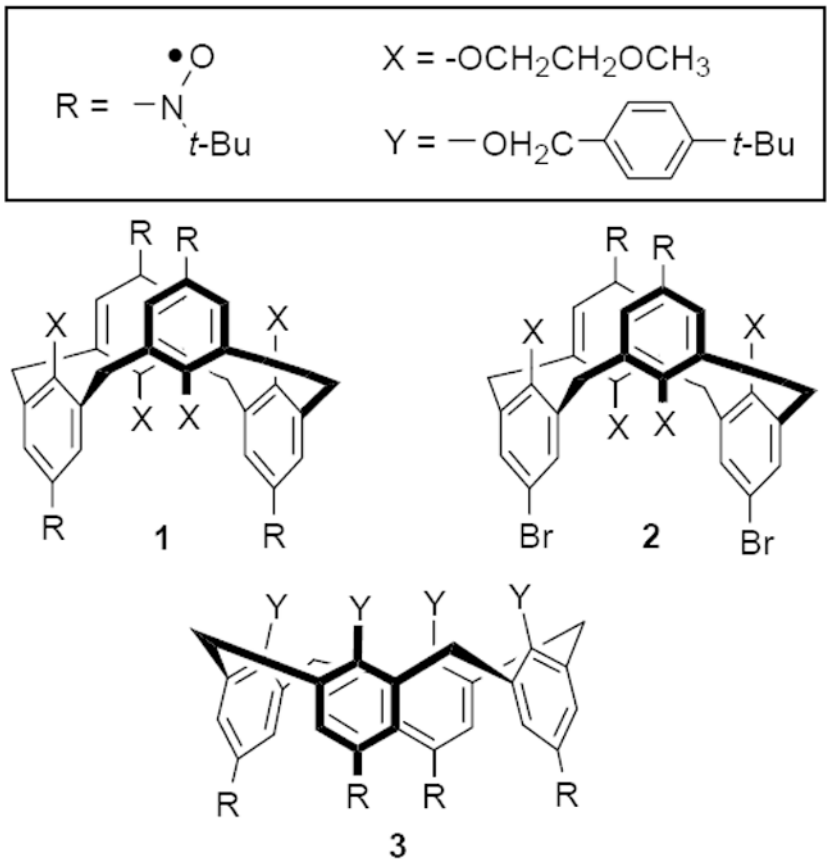

Figure 2.
Nitroxide tetraradical **1** and diradical **2** with the constrained conformations of 1,3-alternate calix[4]arene, and nitroxide tetraradical **3** with the constrained conformation of cone calix[4] arene.

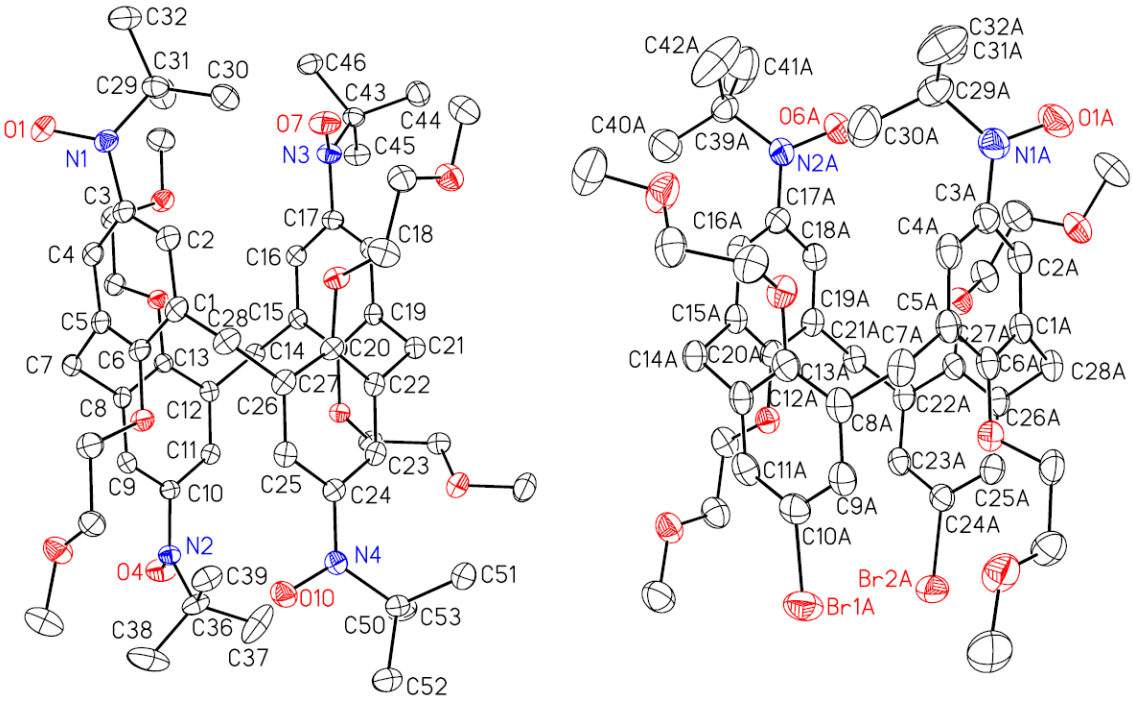

Figure 3.

Molecular structure and conformation for nitroxide tetraradical **1** (left) and diradical **2** (right) with constrained conformations of 1,3-alternate calix[4]arene. Carbon, nitrogen, and oxygens atoms are depicted with thermal ellipsoids set at the 50% probability level. Only one of the two unique molecules of **2** and without the solvent of crystallization (benzene) is shown.

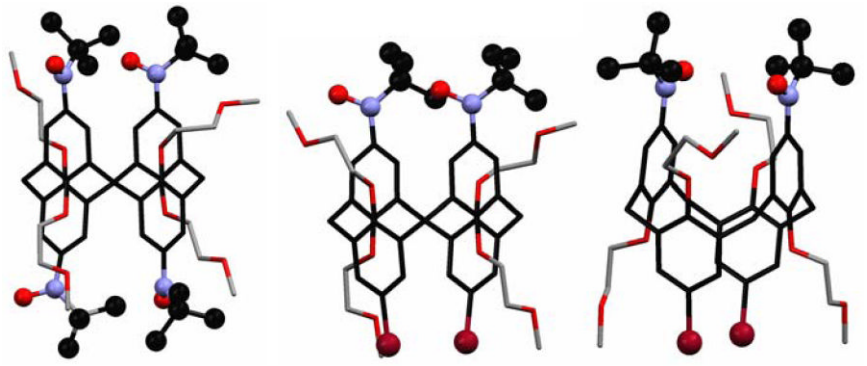

Figure 4.
Conformation of the *tert*-butyl nitroxide moieties (ball-and-stick) in crystalline nitroxide tetraradical **1** and diradical **2**. For **2**, two crystallographically unique molecules are shown; in one of the molecules, disorder in the ethylenoxymethyl chain and the *tert*-butyl group is omitted for clarity.

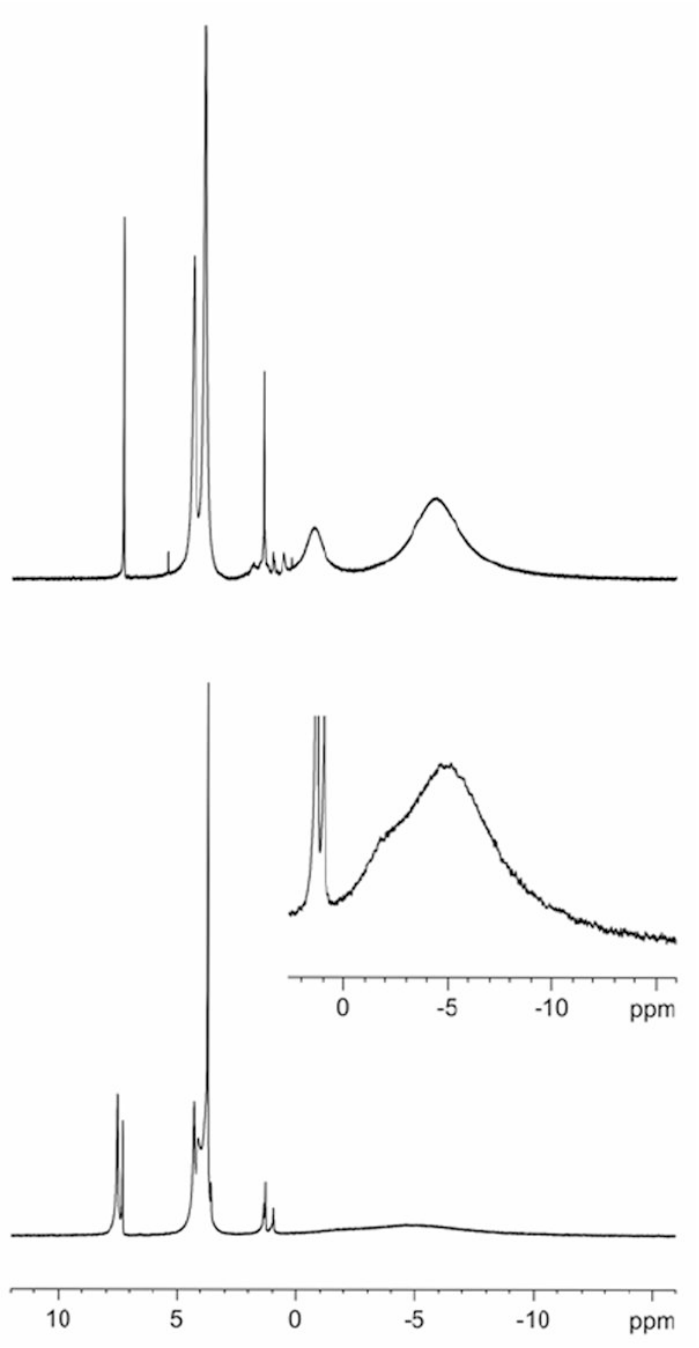

Figure 5.

^{1}H NMR (500 MHz, chloroform-*d*, LB = 1 Hz) spectra for nitroxide tetraradical **1** (top) and diradical **2** (bottom). Inset plot: LB = 10 Hz. The singlets at 7.26 ppm and ~1.5 ppm correspond to the residual non-deuterated chloroform and water peaks. The other sharp, relatively weak peaks are assigned to diamagnetic impurities.

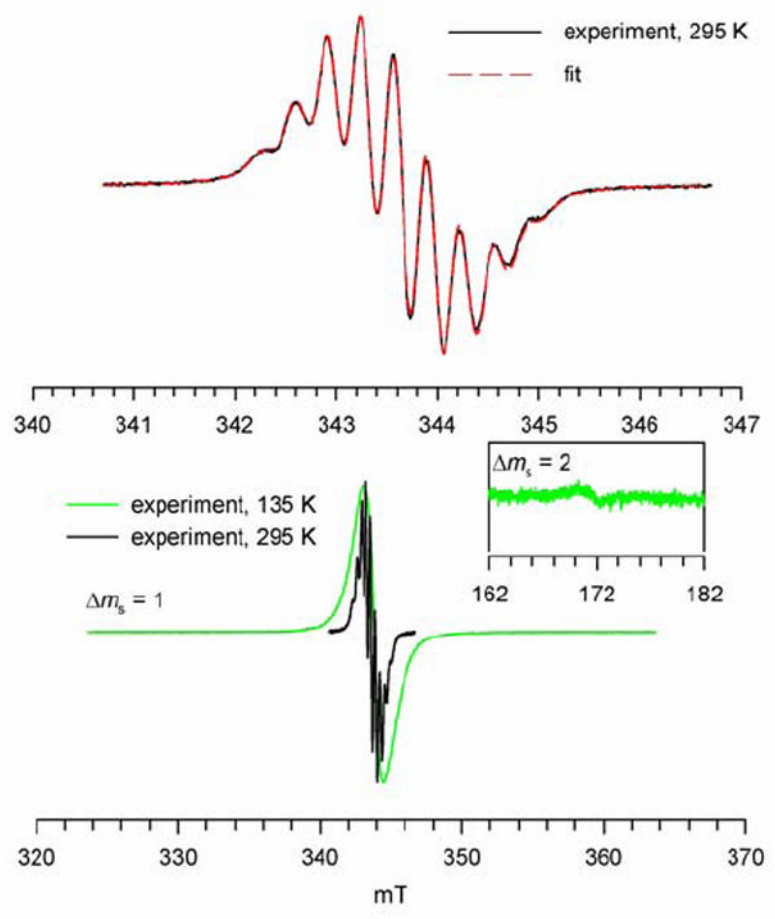

Figure 6.

EPR (X-Band) spectra of **1** in toluene at 295 K and 135 K. Numerical fit (red dashed line) to the experimental spectrum at 295 K corresponds to a single nitroxide tetraradical species; correlation coefficient is 0.999 and the values for the variable parameters are: Lorentzian line width of 0.156 mT, *g*-shift of −0.045 mT (*g*-value = 2.0059), ^{14}N-splitting of 0.319 mT for 4 nuclei, ^{1}H-splitting of 0.048 mT for 8 nuclei.

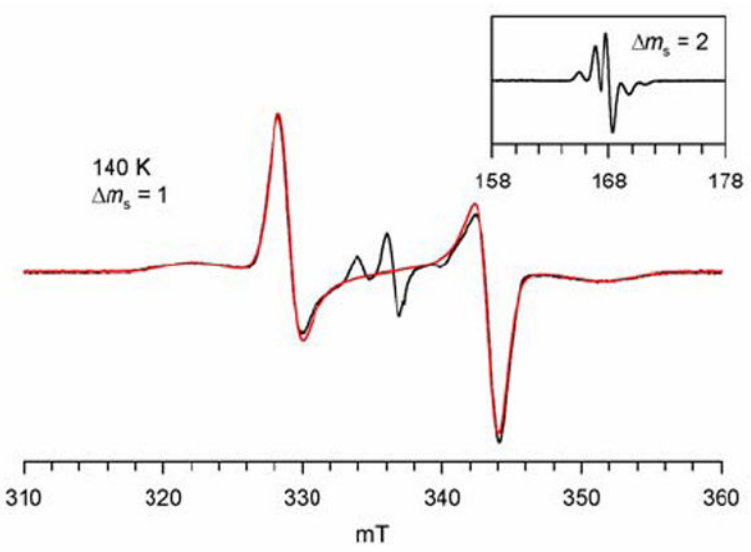

Figure 7.

EPR (X-Band, 9.4424 GHz) spectrum of 0.6 mM nitroxide diradical **2** in toluene/chloroform (4 : 1) at 140 K. The spectral simulation of the $|\Delta m_s| = 1$ region is shown as red trace. The fitting parameters for the spectral simulation to the $S = 1$ state are: $|D/hc| = 1.39 \times 10^{-2}$ cm^{-1} ($|D/g\mu_B| = 14.9$ mT), $|E/hc| = 0$ cm^{-1}, $g_x = 2.0064$, $g_y = 2.0064$, $g_z = 2.0030$, Gaussian line ($L_x = 12$ G, $L_y = 20$ G, $L_z = 40$ G). The center lines correspond to an $S = ½$ (monoradical) impurity.

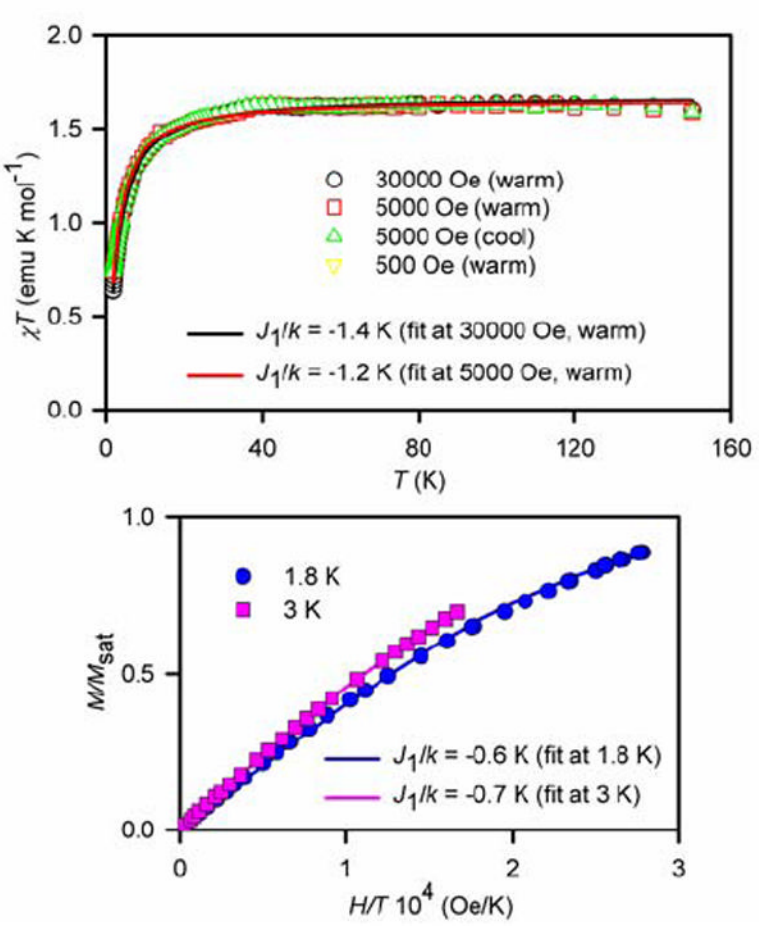

Figure 8.

SQUID magnetometry for 5 mM **1** in THF with numerical fits to the tetraradical model (Figure 10, eq. 1 and 2). For the χT vs. T fits (top) and the M/M_{sat} vs. H/T fits (bottom), the J_2/k (diagonal coupling) is set to −1.1 K and −0.5 K, respectively. The variable parameters (parameter dependence and R^2) are as follows: at 30000 Oe in the warming mode, J_1/k = −1.4 K, w = 1.11 (0.32, 0.998); at 5000 Oe in the warming mode, J_1/k = −1.2 K, w = 1.10 (0.30, 0.995); at 1.8 K, J_1/k = −0.6 K, M_{sat} = 0.76 μ_B (0.85, 0.999); at 3 K, J_1/k = −0.7 K, M_{sat} = 0.86 μ_B (0.97, 1.000).

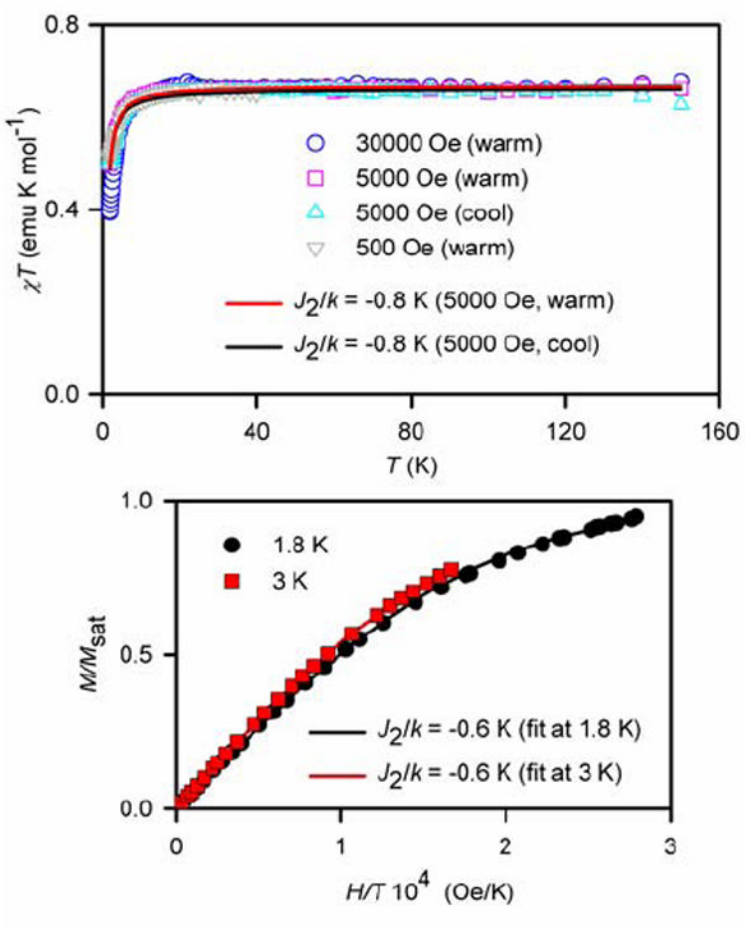

Figure 9.

SQUID magnetometry for 7 mM **2** in THF with numerical fits to the diradical model (eq. 4 with $J_1/k = 0$). For the χT vs. T fits (top) and the M/M_{sat} vs. H/T fits (bottom), the variable parameters (parameter dependence and R^2) are as follows: at 5000 Oe in the warming mode, $J_2/k = -0.8$ K, $w = 0.89$ (0.25, 0.990); at 5000 Oe in the cooling mode, $J_2/k = -0.8$ K, $w = 0.88$ (0.26, 0.982); at 1.8 K, $J_2/k = -0.6$ K, $M_{sat} = 0.80$ μ_B (0.62, 1.000); at 3 K, $J_2/k = -0.6$ K, $M_{sat} = 0.82$ μ_B (0.91, 1.000).

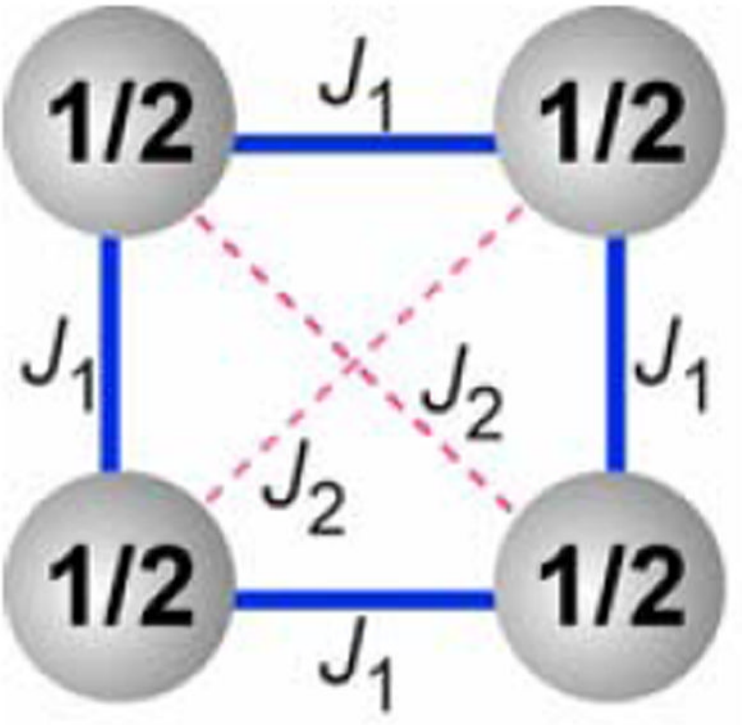

Figure 10.
Cluster of spins $S = ½$ with pairwise exchange couplings J_1 (through-bond) and J_2 (through-space) as the tetraradical model for **1** and **3**. The diradical model for **2** corresponds to a dimer of spins $S = ½$ with pairwise exchange coupling J_2.

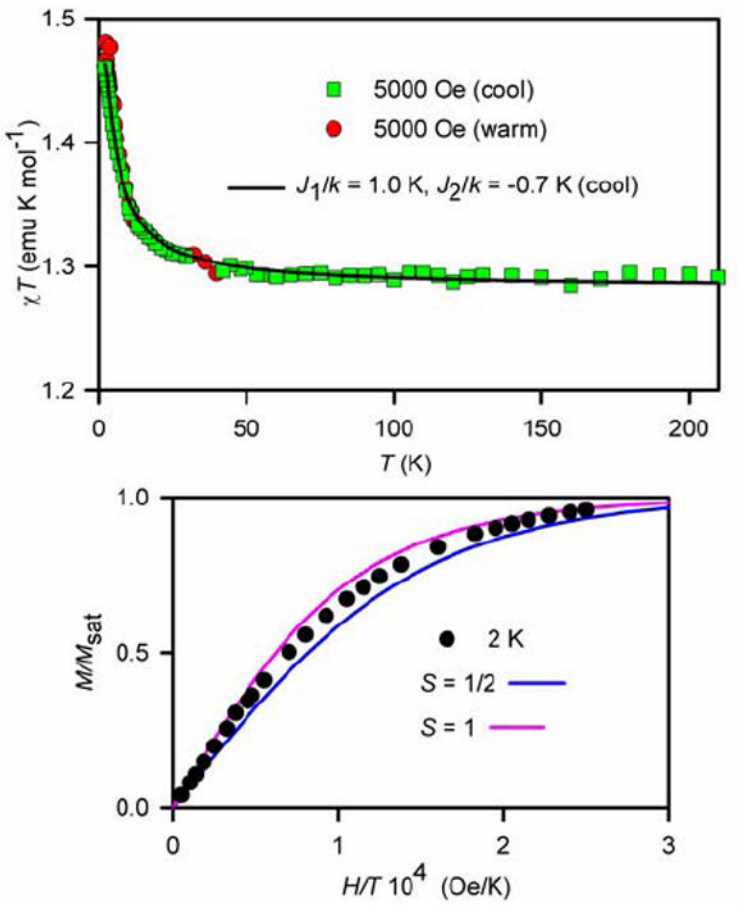

Figure 11.

SQUID magnetometry for 20 mM **3** in 2-MeTHF with numerical fit to the tetraradical model (Figure 10, equation 2). For the χT vs. T plot (top), the variable parameters (parameter dependence) for the numerical fit to tetraradical model at 5000 Oe in the cooling mode are as follows: J_1/k = 1.0 K (0.98), J_2/k = −0.7 K (0.98), w = 0.85 (0.61); R^2 = 0.996. For the M/M_{sat} vs. H/T plot at T = 2 K (bottom), theoretical Brillouin curves for paramagnet with S = ½ and S = 1 are shown.

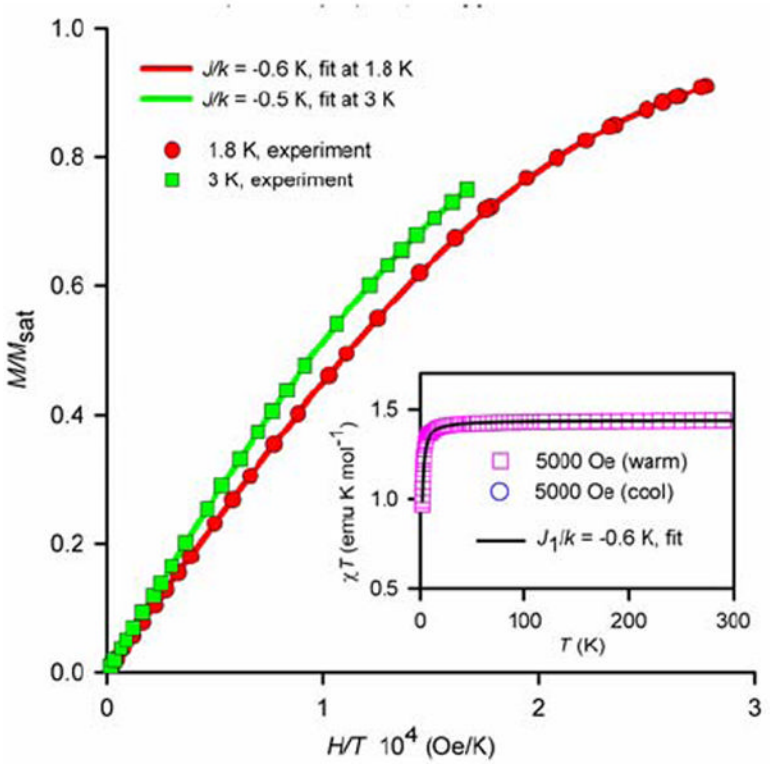

Figure 12.

SQUID magnetometry for solid nitroxide tetraradical **1** with numerical fits to the tetraradical model, using $J_2/k = 0$ (Figure 10, equations 1 and 2). The variable parameters (parameter dependence and R^2) are as follows: at 1.8 K, $J_1/k = -0.6$ K, $M_{sat} = 0.94$ μ_B (0.75, 1.000); at 3 K, $J_1/k = -0.5$ K, $M_{sat} = 0.95$ μ_B (0.94, 1.000); at 5000 Oe in the warming mode, $J_1/k = -0.6$ K, $w = 0.96$ (0.23, 0.993).

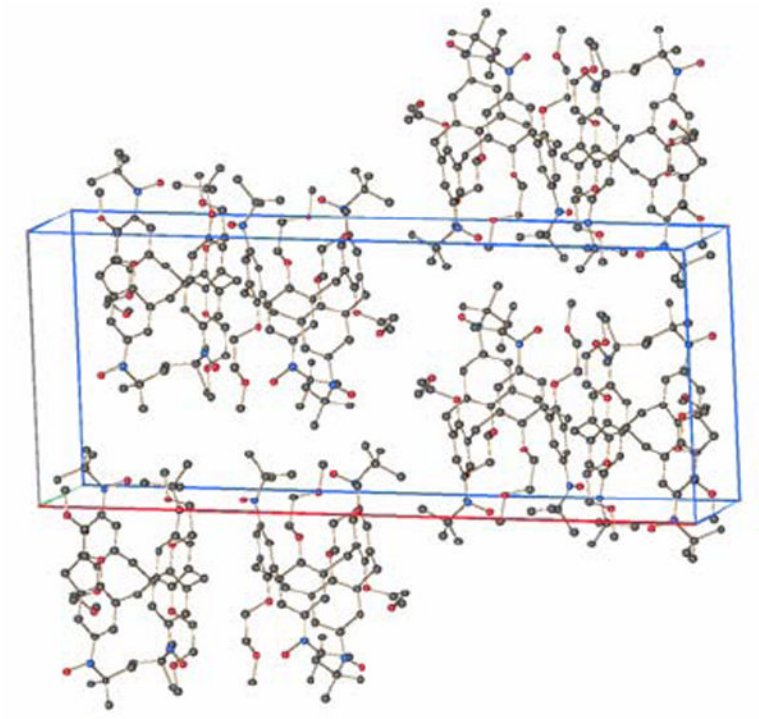

Figure 13.
Crystal packing of nitroxide tetraradical **1**. Hydrogen atoms are omitted for clarity.

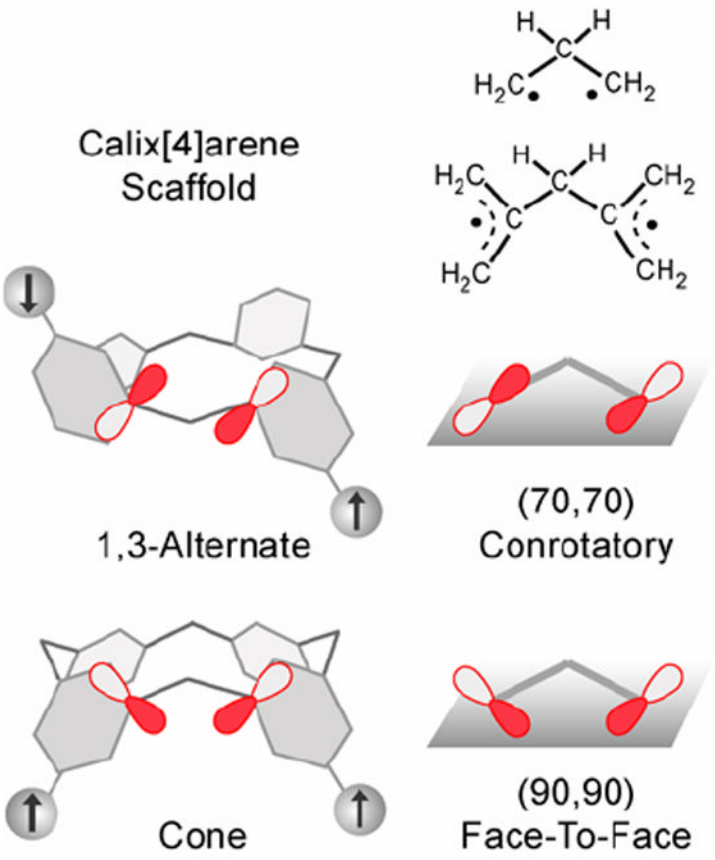

Figure 14.
Relative orientations of the $2p_{\pi}$-orbitals at the *ipso*-positions in the 1,3-alternate and cone calix[4]arene polyradical scaffolds, and the corresponding trimethylene and 2,2'-bis(allyl)methane diradicals.

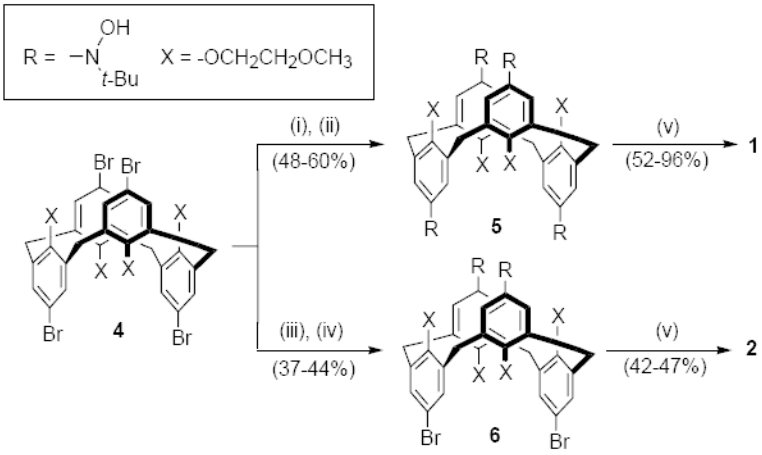

Scheme 1.

Synthesis of nitroxide tetraradical **1** and diradical **2**

Conditions: (i) *t*-BuLi (8 equiv), THF, −78 °C for 2 h, then −20 °C for 15 min; (ii) $[(CH_3)_3CNO]_2$ (2.1 equiv) in THF, −78 °C then slowly warm up to room temperature overnight; (iii) *n*-BuLi (2.2 equiv), THF; (iv) $[(CH_3)_3CNO]_2$ (1.2 equiv); (v) Ag_2O, $CHCl_3$ or CH_2Cl_2.

Table 1

Summary of the X-ray crystallographic data.

property	**1**	**2** (0.25•C_6H_6)
molecular formula	$C_{56}H_{80}N_4O_{12}$	$C_{49.50}H_{63.50}Br_2N_2O_{10}$
formula weight	1001.24	1006.34
crystal/color	red block	red block
crystal system	monoclinic	triclinic
space group	$P2_1/c$	P-1
a, Å	14.920(4)	14.698(5)
b, Å	35.167(9)	19.752(6)
c, Å	10.593(3)	20.370(7)
α, °	90	96.911(9)
β, °	100.379(7)	110.227(9)
γ, °	90	111.428(9)
volume, $Å^3$	5467(2)	4955(3)
Z	4	4
D_{calcd}/g cm^{-3}	1.216	1.349
reflns collected	82665	66102
unique reflns	12675 (R_{int} = 0.0554)	22927 (R_{int} = 0.0627)
data / restraints / parameters	12675 / 0 / 665	22927 / 48 / 1206
R_1 ($I > 2\sigma(I)$)	0.0461	0.0483
wR_2 ($I > 2\sigma(I)$)	0.1141	0.1082
GOF	1.019	1.014

Supporting Information

Exchange Coupling Mediated Through-Bonds and Through-Space in Conformationally-Constrained Polyradical Scaffolds: Calix[4]arene Nitroxide Tetraradicals And Diradical.

Andrzej Rajca,[a] Sumit Mukherjee,[a] Maren Pink,[b] Suchada Rajca[a]*

Department of Chemistry, University of Nebraska, Lincoln, NE 68588-0304. IUMSC, Department of Chemistry, Indiana University, Bloomington, IN 47405.

E-mail address: arajca1@unl.edu

Table of Contents

1. Materials and Special Procedures.

Ether, tetrahydrofuran (THF), and 2-methyltetrahydrofuran (2-MeTHF) for use on the vacuum line were distilled from sodium/benzophenone prior to use. *t*-BuLi was obtained from either Aldrich (1.7 M in pentane) or Acros (1.5 M in pentane); prior to use, their concentrations were determined by titration with *N*-pivaloyl-*o*-toluidine.[S1] Other major commercially available chemicals were obtained from Aldrich. Column chromatography was carried out with flash silica gel, particle size 40–63 μm (EMD Chemicals). Deactivated silica was prepared by stirring flash silica gel with a solution of 2% Et_3N in pentane for 40 – 45 min. The silica gel was then transferred to a column and washed successively with pentane, acetone and pentane, following which it was dried overnight under a steady air pressure (~5 psi). This was then used for the column purifications in the usual way.

25,26,27,28–Tetrahydroxycalix[4]arene was obtained by $AlCl_3$–catalyzed removal of the *tert*-butyl groups from *p-tert*-butylcalix[4]arene according to the literature procedure.[S2] Preparation of 5,11,17,23-tetrabromo-25,26,27,28-tetrakis(methoxyethoxy)calix[4]arene (**4**) in the locked 1,3-alternate conformation is described below.

2. NMR Spectroscopy and Other Analyses.

NMR spectra were obtained using Bruker spectrometers (^{1}H, 500 MHz and 400 MHz) using $CDCl_3$ as solvent. The chemical shift references were as follows: (^{1}H) TMS, 0.0 ppm and (^{13}C) $CDCl_3$, 77.0 ppm. Typical 1D FID was subjected to exponential multiplication with an exponent of 0.1 Hz (for ^{1}H) and 1.0 – 2.0 Hz (for ^{13}C); for selected spectra, both exponential and Gaussian multiplications were used, with exponents indicated as EM and GB for each applicable spectrum.

Values of the magnetic moment and χT were obtained in chloroform using the ^{1}H NMR based Evans method.[S3] Concentric NMR tubes were used (Wilmad, cat. No. WGS-5BL). The outer NMR tube contained a solution of the paramagnetic sample in an approximately 1 : 1 (v/v) mixture of $CDCl_3$ and $CHCl_3$ with accurately determined concentration and the inner concentric tube contained pure $CHCl_3$.

Diamagnetic susceptibility of $CHCl_3$ ($\chi_{dia} = -0.497 \times 10^{-6}$ emu g^{-1}) and Pascal constant correction for the nitroxide diradical (-0.603×10^{-3} emu mol^{-1}) and tetraradical (-0.652×10^{-3} emu mol^{-1}) were used.[S4]

IR spectra were obtained using a Nicolet Avatar 360 FT-IR instrument, equipped with an ATR sampling accessory (Spectra Tech, Inc.). A few drops of the compound in CH_2Cl_2 were applied to the surface of a ZnSe ATR plate horizontal parallelogram (45°, Wilmad). After the solvent evaporated, the spectrum was acquired (128 scans, 4-cm^{-1} resolution).

MS analyses were carried out at the Nebraska Center for Mass Spectrometry.

Table S1. Summary of variable temperature ^{1}H NMR (400 MHz) spectroscopic studies of tetrahydroxylamine **5** (C_2Cl_4/benzene-d_6) and dihydroxylamine **6** (chloroform-*d*).

Chemical shifts (Hz)			Temperatures (° C)		k_{coal} (s^{-1})	$\Delta G^{\ddagger}$ (kcal mol^{-1})
ν_1	ν_2	$\nu_1-\nu_2$	$T_{slow\ exchange}$	$T_{coalescence}$		
Tetrahydroxylamine **5**						
2953.6	2685.2	268.4	25	52	597	14.8
Dihydroxylamine **6**						
2926.4	2907.2	19.2	−30	5	44.6	14.1
2953.2	2716.4	238.8	−30	33	526	14.1

3. X-ray Crystallography of 1 and 2.

All data were collected on Bruker SMART system at IUMSC (Indiana University). Data collection, structure solution, and refinement are briefly summarized below; more detailed description may be found in the accompanying crystallographic information files (CIFs). The single crystals for the X-ray crystallographic studies were obtained via slow evaporation of solvent at room temperature: nitroxide tetraradical **1** (label: SM-5-4recry) and diradical **2** (label: SM-5-5recry).

Data collection, structure solution and refinement. All data collections were carried out using Mo Kα radiation (λ = 0.71073 Å, graphite monochromator) at 137 K. The intensity data were corrected for absorption.[S5] Final cell constants were calculated from the xyz centroids of strong reflections from the actual data collection after integration.[S6]

Space groups were determined based on intensity statistics and systematic absences. Structures were solved with direct methods using SIR-92[S7] and refined with full-matrix least squares / difference Fourier cycles using SHELXL-97.[S8] All non-hydrogen atoms were refined with anisotropic displacement parameters. The hydrogen atoms were placed in ideal positions and refined as riding atoms with relative isotropic displacement parameters.

Nitroxide tetraradical 1. The compound crystallized in space group P21/c with one molecule per asymmetric unit. The final full matrix least squares refinement converged to R1 = 0.0461 and wR2 = 0.1276 (F2, all data). The remaining electron density was located on bonds.

Nitroxide diradical 2. The compound crystallized in space group P-1 with two molecules and one half solvent molecule (benzene) per asymmetric unit. The final full matrix least squares refinement converged to R1 = 0.0483 and wR2 = 0.1257 (F2, all data). The remaining electron density is located near the bromine atoms. Disorder was observed for a *tert*-butyl group and methoxyethylene; they were refined with a set of appropriate restraints and constraints.

Table S2. Dihedral angles between the planes defined by the C(*ipso*)-C(CH_2)-C(*ipso*) and benzene ring planes (illustrated as triangles and hexagons) for nitroxide tetraradical **1** and diradical **2**.

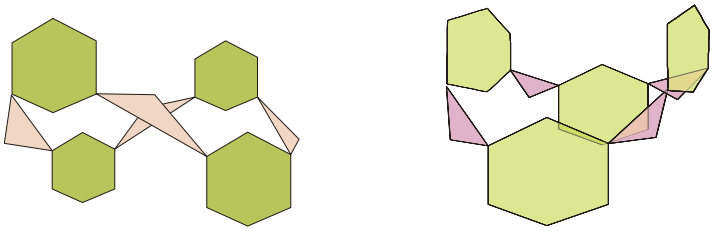

Nitroxide tetraradical **1**

Plane to plane (defined by the following carbon atoms)	Angle (plane to plane) [°]
Ph 1-6 to 5,7,8	115.7 (or 64.3)
5,7,8 to Ph 8-13	118.4 (or 61.6)
Ph 8-13 to 12,14,15	114.3 (or 65.7)
12,14,15 to Ph 15-20	61.5
Ph 15-20 to 19,21,22	67.5
19,21,22 to Ph 22-27	64.3
Ph 22-27 to 26,28,1	67.9
26,28,1 to Ph 1-6	120.8 (or 59.2)

Nitroxide diradical **2**

Molecule A

Plane to plane (defined by the following carbon atoms)	Angle (plane to plane) [°]
Ph 1-6 to 5,7,8	68.0
5,7,8 to Ph 8-13	70.2
Ph 8-13 to 12,14,15	107.4 (or 72.6)
12,14,15 to Ph 15-20	65.0
Ph 15-20 to 19,21,22	65.1
19,21,22 to Ph 22-27	69.9
Ph 22-27 to 26,28,1	72.4
26,28,1 to Ph 1-6	114.4 (or 65.6)

Molecule B

Plane to plane (defined by the following carbon atoms)	Angle (plane to plane) [°]
Ph 1-6 to 5,7,8	111.6 (or 68.4)
5,7,8 to Ph 8-13	70.3
Ph 8-13 to 12,14,15	73.4
12,14,15 to Ph15-20	66.1
Ph 15-20 to 19,21,22	113.9 or 66.1
19,21,22 to Ph 22-27	69.4
Ph 22-27 to 26,28,1	70.0
26,28,1 to Ph 1-6	70.4

4. EPR Spectroscopy of 1 and 2, and Magnetic Studies of 1, 2, and 3.

EPR spectroscopy. CW X-band EPR spectra for **1** and **2** in solution were acquired on Bruker EMX instrument, equipped with a frequency counter and nitrogen flow temperature control (130–320 K). The samples were contained in the 4-mm O.D. EPR quartz tubes, equipped with high-vac PTFE stopcocks. Solvent was vacuum transferred into the tube, to form a homogeneous solution after attaining ambient temperature. Spectra were obtained using dual mode cavity, with the oscillating magnetic field perpendicular (TE_{102}) to the swept magnetic field. The *g*-values were referenced using DPPH (g = 2.0037, powder, Aldrich).

For distance (r, in Å) measurements based upon Eaton's equation (eq. S1), the relative intensities of the the $|\Delta m_s| = 1$ and $|\Delta m_s| = 2$ regions for 1 mM diradical **2** in toluene/chloroform were obtained by double integration with baseline correction; intensity of the monoradical was negligible. The instrument settings for the $|\Delta m_s| = 2$ region were as follows: microwave (MW) power attenuation = 10 dB (power = 20.4 mW) and receiver gain = 5×10^5; analogous settings for the $|\Delta m_s| = 1$ region were 40 dB (2.046×10^{-2} mW) and 1×10^5. Except for the center fields, all other settings, including MW frequency (ν = 9.4848 GHz), modulation amplitude (2 G), number of scans, and sweep width (600 G), were identical.

$$\text{relative intensity} = [19.5 \times (9.1)^2]/r^6\nu^2 \qquad \text{(S1)}$$

SQUID Magnetometry. Quantum Design (San Diego, CA) MPMS5S (with continuous temperature control) was used. All samples were contained in home-made 5-mm O.D. EPR quality quartz tubes, modified to possess a thin bottom, which is 6 cm from the end of the tube.[S9]

For solution samples, tetraradical **1**, diradical **2**, or tetraradical **3** were loaded into the tube, placed under vacuum, and then solvents were vacuum transferred. The tube was flame sealed under vacuum. The samples were carefully inserted to the magnetometer, with the sample chamber at 290–300 K. The sequence of measurements started with a cooling mode from 300 K to 1.8 K, and then followed with the other sequences of measurements below the melting point of the solution (1.8–150 K). Correction for diamagnetism was carried out by extrapolation of the χ vs. $1/T$ plots, typically, from the 60–140 K

temperature range (R^2 = 0.9999). However, for selected samples in 2-methyltetrahydrofuran, a wider temperature range (up to the temperature of 240 K) was used. Usually the cooling mode data, with 10–60 s delays, after a "stable temperature" was indicated by the MPMS at each temperature, were used for such extrapolations.

For solid state samples, **1** or **2** was loaded to the tube, placed under vacuum, and then flame sealed under partial pressure of helium gas. For one of the samples of tetraradical **1** (Figure 12), following the measurements, the SQUID sample tube was opened and cleaned, and then identical sequences of measurements were carried out for the point-by-point correction for diamagnetism; additional corrections were based upon Pascal constants, scaled by a factor of 0.9, i.e., $\chi_{dia} = 0.9\times6.52\times10^{-4}$ emu mol^{-1}. For all other samples of solid di- and tetraradicals, the correction for diamagnetism was based upon high temperature extrapolation of the χ vs. $1/T$ plots, i.e., a suitable numerical factor (M_{dia}) was added to the magnetization (M), until the χT vs. T plot becomes flat in the high temperature range.

EPR Spectral Simulations and Numerical Curve Fitting for SQUID Magnetic Data. The WINEPR SimFonia program (Version 1.25, Bruker) was used for spectral simulations of nitroxide diradical **2** in rigid matrices. WinSIM program (Public EPR Software Tools, D. A. O'Brien, D. R. Duling, Y. C. Fann) was used for numerical fitting of solution phase EPR spectra.

The SigmaPlot for Windows software package was used for numerical curve fitting of the magnetic data. The reliability of a fit is measured by the parameter dependence, which is defined as follows: *dependence = 1 – ((variance of the parameter, other parameters constant)/(variance of the parameter, other parameters changing))*. Values close to 1 indicate an overparametrized fit. The quality of fits is measured by a coefficient of determination (R^2), which is defined for nonlinear numerical fits of the magnetic data as follows (eq. S2):

$$R^2 = 1 - [(\Sigma(y_i - Y_i)^2)/(\Sigma(y_i - \langle y \rangle)^2)] \qquad \text{(S2)}$$

where y_i, Y_i , and $\langle y \rangle$ denote experimental values, fitted values, and the arithmetic mean of the experimental values. Values close to 1 indicate a fit of high quality.

5. Alternative Models for Numerical Fitting of Magnetic Data for Tetraradical 1 and Diradical 2.

Two diradicals model. In this model, it is assumed that all nitroxide moieties are involved in only one dominant pairwise antiferromagnetic exchange coupling (J/k). For isolated **1** and **2**, this model describes pairwise exchange couplings between the diagonal nitroxides only. For solid **1** and **2**, the four nitroxide moieties are described as two diradicals. For tetraradical **1**, equations for the field-dependence of magnetization (M vs. H) and temperature dependence of magnetic susceptibility (χT vs. T) are provided (eq. S3, eq. S4a). N denotes the number of moles of tetraradical **1** (eq. S3). Also, impurities and inaccuracies in the mass balance are accounted for by the "magnetization at saturation," M_{sat} (eq. S3) and the mass factor, w (eq. S4a). Both equations account for paramagnetic saturation. A similar model may be used to fit the χT vs. T data for diradical **2** (eq. S4b).

$$M = (11180N)M_{sat}[F_1 + F_2] \quad \text{(S3)}$$

$$\chi T = (1.118T/H)w[F_1 + F_2] \quad \text{(S4a)}$$

$$\chi T = (1.118T/2H)w[F_1 + F_2] \quad \text{(S4b)}$$

$$F_n = [2\sinh(a)]/[1 + 2\cosh(a) + \exp((-2J_n/k)/T)];\ n = 1, 2$$

$$a = 1.345(H/T);\ J_1 = J_2$$

It should be noted that the replacement of the $J_2 = 0$ restraint in equations S5, S6a, and S6b with a $J_1 = J_2$ restraint gives equations S3, S4a, and S4b. Also, setting $J_1 = 0$ in the tetraradical model (eq. 1, 2, and 4, maint text) gives equations (and numerical fits) that are identical to equations S3, S4a, and S4b. Still another option is a three-parameter fit, using eq. S4a with $J_1 \neq J_2$ (e.g., ref 32, main text), for tetraradical **1**.

Diradical plus two S = ½ monoradicals model. In this model, it is assumed that one half of the nitroxide moieties may be described as exchange-coupled diradicals and the other half of the nitroxide moieties are treated as independent S = ½ monoradicals. In other words, the four nitroxide moieties in solid **1** and **2** could be described as one diradical plus two S = ½ monoradicals.

For tetraradical **1**, both temperature-dependence (χT vs. T) and field-dependence (M vs. H) of the experimental magnetic data are well fit by the model of "one diradical plus two S = ½ monoradicals", with antiferromagnetic exchange coupling (J/k) in the "diradical" (eq. S5 and eq. S6a). N denotes number of moles of tetraradical **1** (eq. S5). Also, impurities and inaccuracies in the mass balance are accounted for by the "magnetization at saturation," M_{sat} (eq. S5) and the mass factor, w (eq. S6a). Both equations account for paramagnetic saturation. Similar model may be used to fit the χT vs. T data for diradical **2** (eq. S6b).

$$M = (11180N)M_{sat}[F_1 + F_2] \quad \text{(S5)}$$

$$\chi T = (1.118T/H)w[F_1 + F_2] \quad \text{(S6a)}$$

$$\chi T = (1.118T/2H)w[F_1 + F_2] \quad \text{(S6b)}$$

$$F_n = [2\sinh(a)]/[1 + 2\cosh(a) + \exp((-2J_n/k)/T)];\ n = 1, 2$$

$$a = 1.345(H/T);\ J_2 = 0$$

Two-parameter numerical fits (eq. S5, S6a, and S6b) for tetraradical **1** and diradical **2** give similar antiferromagnetic exchange coupling, $J/k \approx -1.8$ K, between isolated pairs of nitroxide moieties.

6. Preparation of Tetrabromocalix[4]arene 4.

25,26,27,28-Tetrakis(methoxyethoxy)calix[4]arene. To a mixture of 2-methoxyethanol (22.85 g, 300 mM, sm-4-19) and 40 mL of dry pyridine, *p*-TsCl (63 g, 330 mM) was added in portions, in such a way that the temperature of the reaction mixture did not exceed 20 ºC. The stirring was continued for 6 h, after which the reaction mixture was taken up in ether and water, and then the ether layer was washed thoroughly with water. Then it was dried over $MgSO_4$ and the ether was removed under reduced pressure. The resulting 2-methoxyethyl tosylate (yellow oil) was used without further purification. Similarly, four additional reactions (sm-4-27, sm-4-89, sm-6-53, sm-6-72) on 25-g scales gave the crude

product with the estimated purity of 90–92% by ^{1}H NMR spectroscopy. The yields of these crude products were in the 60–72% range.

A mixture of 25,26,27,28-tetrahydroxycalix[4]arene (2.00 g, 4.71 mmol) and Cs_2CO_3 (46.1 g, 0.141 mol) in DMF (110 mL) was stirred at 80 °C for 30 min. Subsequently 2-methoxyethyl tosylate (32.7 g, 0.141 mol) was added and the reaction mixture was kept at 80 °C for 5 h. Upon cooling to ambient temperature, the reaction mixture was poured into water (400 mL). After extraction with CH_2Cl_2 (3 × 125 mL), the combined organic layers were washed with 1 N HCl (1 × 125 mL) and brine (3 × 125 mL). In order to remove the excess tosylate, a mixture of the resulting residue, KI (2 g), and Et_3N (2 mL) in CH_3CN (60 mL) was refluxed for 1 h. The solvent was removed in vacuo. CH_2Cl_2 (100 mL) was added to the residue whereupon the organic layer was washed with 1 N HCl (1 × 100 mL) and water (2 × 125 mL). The organic layer was dried over $MgSO_4$. Concentration in vacuo gave a brown gel-like solid which was triturated with cold MeOH to afford a white solid (1.39 g, 45%, m.p. 197–199 °C; lit.[S10] 198–200 °C). In three additional reactions carried out on 1-g, 1.5-g, and 0.1-g scale, the product of trituration was further recrystallized from CH_2Cl_2/MeOH, to provide the product in 46–48% (lit.[S10] 76%) yields. ^{1}H NMR (500 MHz, $CDCl_3$): 7.070 (d, J = 7.0, 8H), 6.710 (t, J = 7.0, 4H), 3.786 (t, J = 5.0, 8H), 3.478 (t, J = 5.0, 8H), 3.648 (s, 8H), 3.388 (s, 12H).

5,11,17,23-Tetrabromo-25,26,27,28-tetrakis(methoxyethoxy)calix[4]arene (4).[S11] N-bromosuccinimide (5.7 g, 31.9 mmol) and 25,26,27,28-tetrakis(methoxyethoxy)calix[4]arene (2.38 g, 3.62 mmol) in methyl ethyl ketone (115 mL) were stirred at room temperature for 24 h. Subsequently, $NaHSO_3$ (5 mL, 10% in water) was added to the stirred reaction mixture. The aqueous workup with CH_2Cl_2 (25 mL), drying over $MgSO_4$, concentration in vacuo, and recrystallization of the crude in CH_2Cl_2/MeOH gave white crystals (2.92 g, 83%, m.p. 255 °C, sm-6-60). From other five reactions carried out on 100-mg (sm-4-34), 588-mg (sm-4-40), 750-mg (sm-4-88), 1.4-g (sm-5-7), and 1.3-g (sm-5-97) scale, tetrabromocalix[4]arene **4** was obtained in 81–93% yields. The higher yields correspond to the crude mixtures, which were of sufficient purity (>95% based upon ^{1}H NMR spectra) for the

subsequent steps in the synthesis. ^{1}H NMR (500 MHz, $CDCl_3$, sm-6-60recry1): 7.312 (s, 8H), 3.853 (m, 8H), 3.734 (m, 8H), 3.595 (s, 8H), 3.456 (s, 12H). ^{13}C NMR (125 MHz, $CDCl_3$, sm-6-60recry1): 154.6, 134.6, 133.2, 114.9, 71.94, 71.91, 59.3, 34.1. IR (ZnSe, cm^{-1}, sm-6-60recry1): 2918, 2880, 1577, 1450, 1365, 1195, 1130, 1050, 852. LR/HR FABMS (3-NBA, sm-6-60recry1): m/z (ion type, % RA in the *m*/*z* 700–1400, deviation for the formula) at 975.9721 ($[M+8]^+$, 29, –3.5 ppm for $^{12}C_{40}H_{44}{}^{16}O_8{}^{81}Br_4$), 973.9657 ($[M+6]^+$, 61, 5.2 ppm for $^{12}C_{40}H_{44}{}^{16}O_8{}^{81}Br_3{}^{79}Br$), 971.9660 ($[M+4]^+$, 100, 7.0 ppm for $^{12}C_{40}H_{44}{}^{16}O_8{}^{81}Br_2{}^{79}Br_2$), 969.9664 ($[M+2]^+$, 62, 8.8 ppm for $^{12}C_{40}H_{44}{}^{16}O_8{}^{81}Br^{79}Br_3$), 967.9737 ($[M]^+$, 16, 3.3 ppm for $^{12}C_{40}H_{44}{}^{16}O_8{}^{79}Br_4$).

7. Acknowledgment

The packing plots in Figures S1 – S3 were prepared using Mercury1.3 program from CCDC.

8. References for Supporting Information

S1. Suffert, J. *J. Org. Chem.* **1989**, *54*, 509–510.

S2. Gutsche, C.D.; Levine, J. A., Sujeeth, P. K. *J. Org. Chem.* **1985**, *50*, 5802–5806.

S3. Evans, D. F. *J. Chem. Soc.* **1959**, 2003–2005. Live, D. H.; Chan, S. I. *Anal. Chem.* **1970**, *42*, 791–792.

S4. *Handbook of chemistry and physics*, CRC Press, INC, Florida, 1983–1984, 64th Ed., E-114.

S5. SADABS: Blessing, R. *Acta Cryst. A* **1995**, *51*, 33–38).

S6. SAINT 6.1, Bruker Analytical X-Ray Systems, Madison, WI, **1999**.

S7. SIR-92: Altomare, A.; Cascarno, G.; Giacovazzo, C.; Gualardi, A. *J. Appl. Cryst.* **1993**, *26*, 343–350.

S8. SHELXL-97: SHELXTL-Plus V5.10, Bruker Analytical X-Ray Systems, Madison, WI

S9. Rajca, A.; Pink, M.; Rojsajjakul, T.; Lu, K.; Wang, H.; Rajca, S. *J. Am. Chem. Soc.* **2003**, *125*, 8534–8538.

S10. Verboom, W.; Datta, S.; Reinhoudt, D. N. *J. Org. Chem.* **1992**, *57*, 5394–5398.

S11. Mislin, G.; Graf, E, Hosseini, M. W.; Cian, A. D.; Kyritsakas, N. *Chem. Commun.* **1998**, 2545–2546.

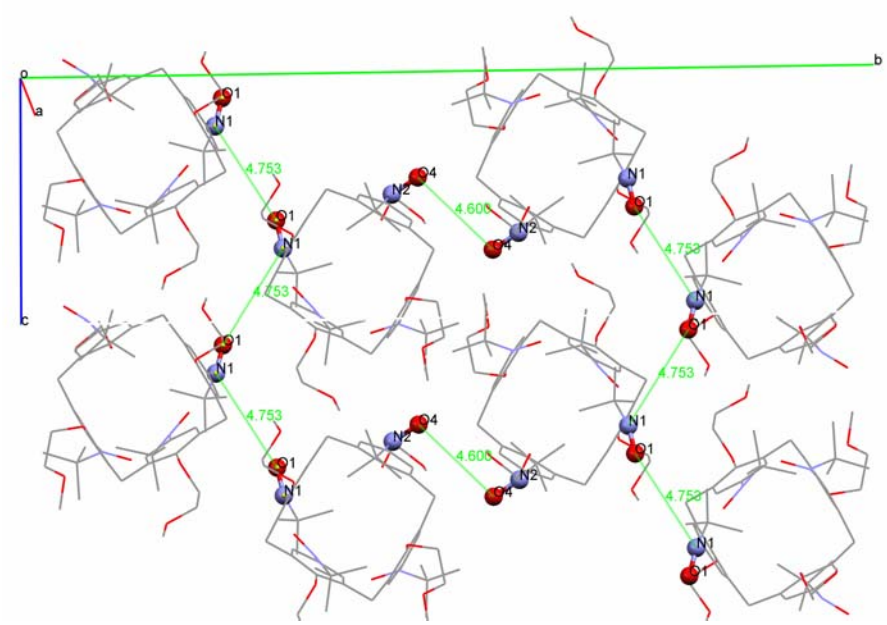

Figure S1. Crystal packing of **1** as viewed in the approximate direction of the crystallographic *a*-axis. The NO groups, with the short intermolecular O···O and N···O distances of 4.60 and 4.75 Å, are shown in ball-and-stick. Hydrogen atoms are omitted for clarity.

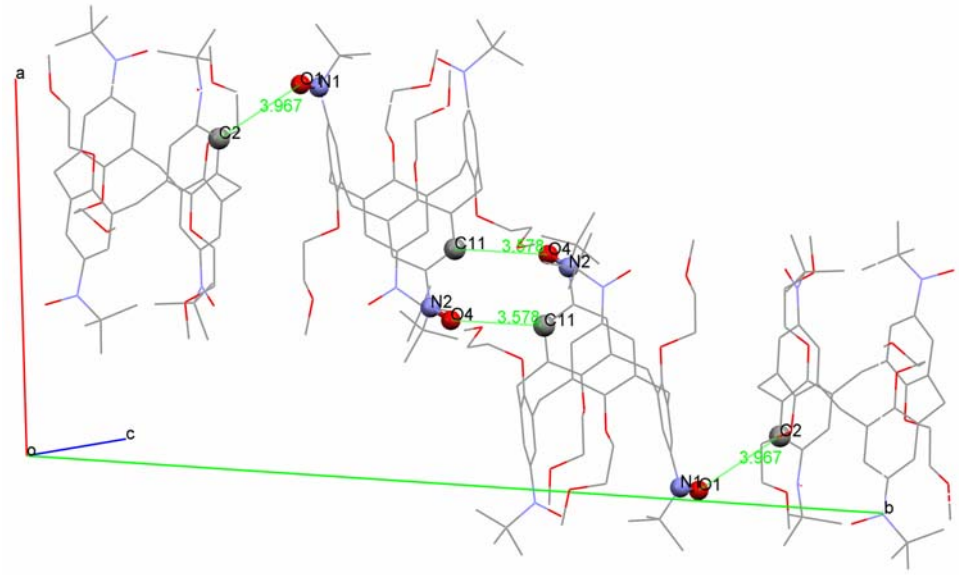

Figure S2. Crystal packing of **1** as viewed in the approximate direction of the crystallographic *c*-axis. The NO groups and carbon atoms, with the short intermolecular O···C distances (O1···C2 = 3.97 Å and O4···C11 = 3.58 Å), are shown in ball-and-stick. Hydrogen atoms are omitted for clarity.

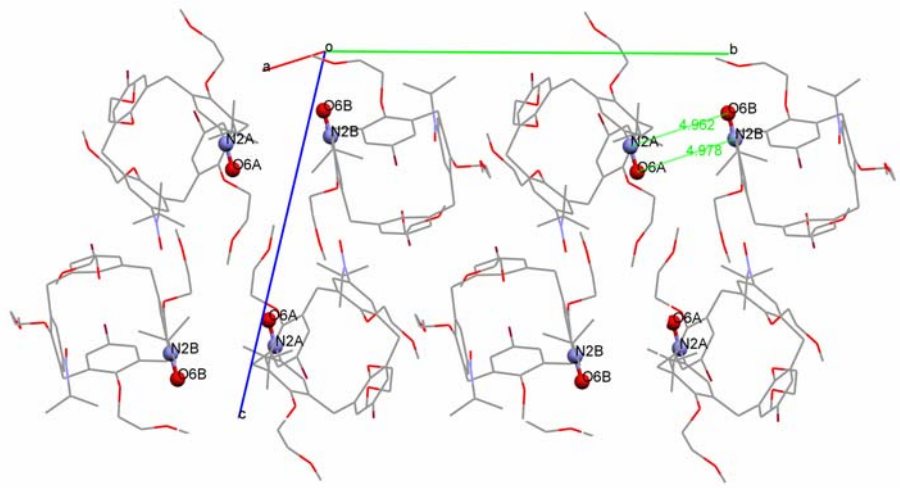

Figure S3. Crystal packing of **2** as viewed in the approximate direction of the crystallographic *a*-axis. The NO groups forming intermolecular dimers are shown in ball-and-stick; the short intermolecular N···O distances of 4.96 and 4.98 Å are found. Both angles and torsions are within 5° of the values expected for a rectangular arrangement of the NO groups within the dimer. Hydrogen atoms, disorder, and solvent of crystallization (benzene) are omitted for clarity.

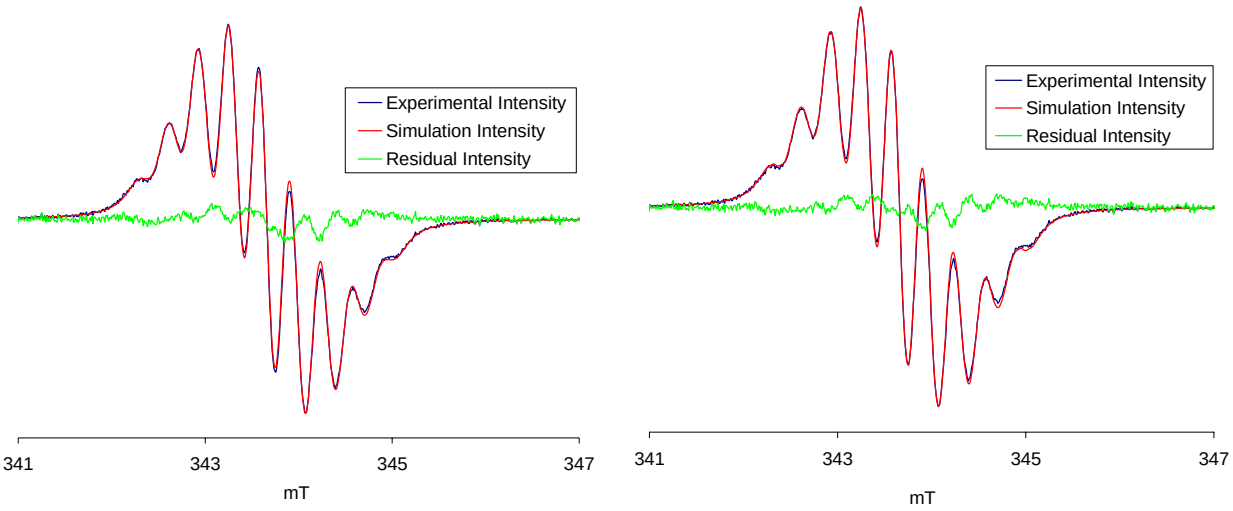

Figure S4. EPR (X-band) spectra of 1 mM nitroxide tetraradical **1** in toluene at room temperature.

Left spectrum, red trace: single species numerical fit (R = 0.999, WinSim), as shown in Figure 6 (main text), with the following variable parameters [rel. concentration, Lorentzian percentage, line width, g-shift (g-value), ^{14}N-splitting (spin, number), ^{1}H-splitting (spin, number)]: species no. 1 [100, 100%, 1.560, −0.450 (2.0059), 3.190 (1, 4), 0.480 (0.5, 8)]. Right spectrum (ks980r2), red trace: three-species numerical fit (R = 0.999, WinSim) with the following variable parameters [rel concentration, Lorentzian percentage, line width, g-shift (g-value), ^{14}N-splitting (spin, number), ^{1}H-splitting (spin, number)]: species no. 1 [98.7, 100%, 1.510, −0.450 (2.0059), 3.190 (1, 4), 0.490 (0.5, 8)], species no. 2 [1.1, 100%, 1.510, −0.400 (2.0058), 4.330 (1, 3), 0.620 (0.5, 6)], species no. 3 [0.2, 100%, 0.510, −0.500 (2.0059), 6.570 (1, 2), 0.800 (0.5, 4)]. The line widths, g-shifts, and hyperfine splittings are reported in Gauss. Green trace: Residual Intensity (the difference between Experimental Intensity and Simulation Intensity multiplied by a factor of 2).

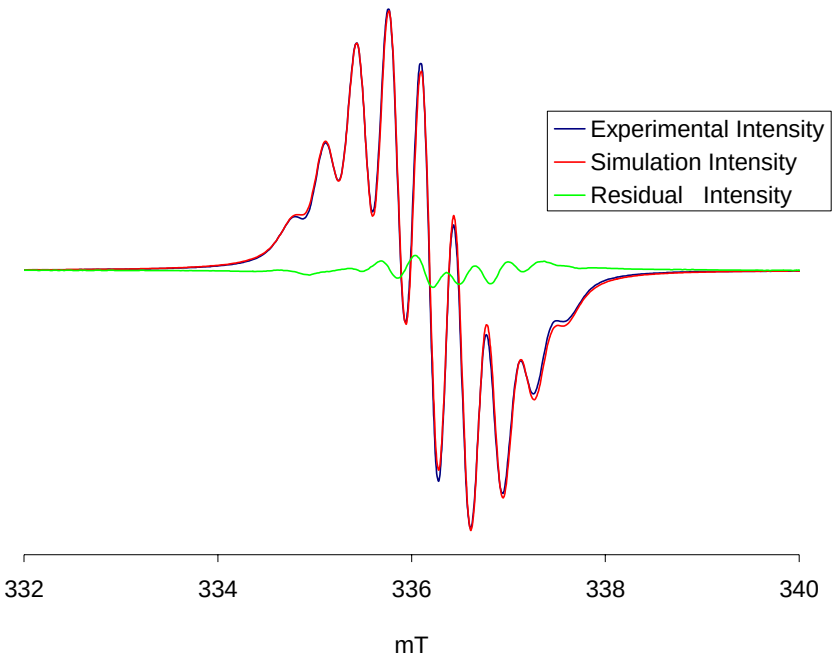

Figure S5. EPR (X-band) spectra of 0.6 mM nitroxide tetraradical **1** in toluene/chloroform (4 : 1) at 296 K (PT366r1). Red trace: single species numerical fit (R = 0.999, WinSim), with the following variable parameters [rel. concentration, Lorentzian percentage, line width, g-shift (g-value), ^{14}N-splitting (spin, number), ^{1}H-splitting (spin, number)]: species no. 1 [100, 100%, 1.680, 3.780 (2.0056), 3.290 (1, 4), 0.390 (0.5, 8)]. The line widths, g-shifts, and hyperfine splittings are reported in Gauss. Green trace: Residual Intensity (Experimental Intensity−Simulation Intensity)

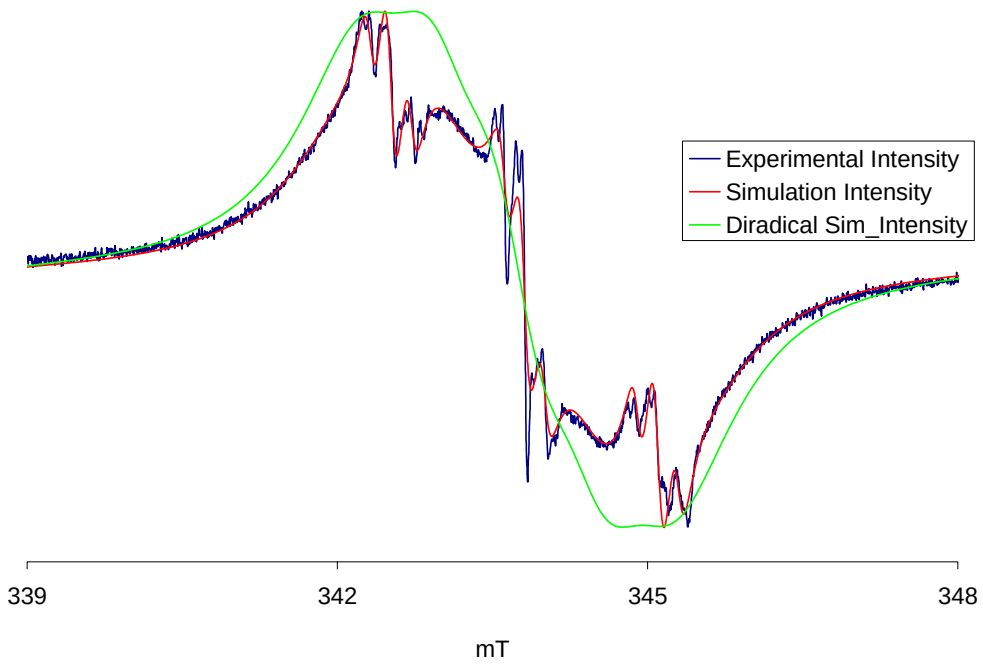

Figure S6. EPR (X-band) spectrum of 1.1 mM nitroxide diradical **2** in toluene at 295 K (KS1263r3). Red trace: numerical fit (R = 0.994, WinSim) with the following variable parameters [rel concentration, Lorentzian percentage, line width, g-shift (g-value), ^{14}N-splitting (spin, number), ^{1}H-splitting (spin, number)]: species no. 1 [97.880, 100%, 7.860, −0.550 (2.0064), 6.520 (1, 2)], species no. 2 [2.120, 80%, 1.080, 0.070 (2.0060), 12.910 (1, 1), 1.970 (0.5, 2)]. The ^{1}H-splitting for the diradical was not included. The line widths, g-shifts, and hyperfine splittings are reported in Gauss. Green trace: numerical fit for species no. 1 in isolation with above optimized parameters.

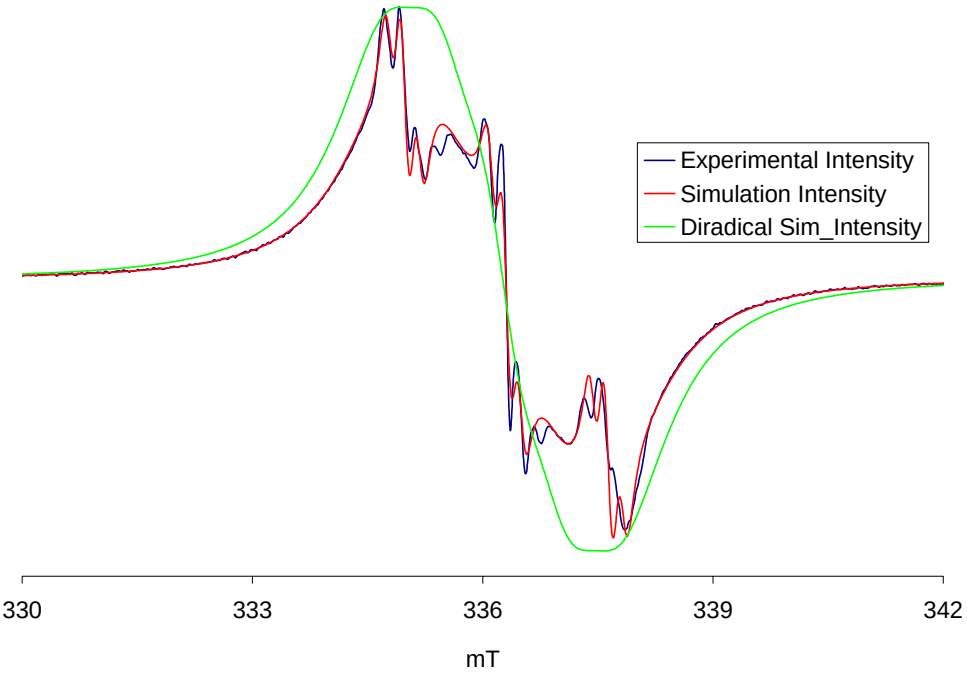

Figure S7. EPR (X-band) spectrum of 0.65 mM nitroxide diradical **2** in toluene/chloroform (4 : 1) at 296 K (PT364r1). Red trace: numerical fit (R = 0.995, Winsim) with the following variable parameters [rel concentration, Lorentzian percentage, line width, g-shift (g-value), ^{14}N-splitting (spin, number), ^{1}H-splitting (spin, number)]: species no. 1 [97.060, 99%, 8.290, 4.520 (2.0061), 6.570 (1, 2)], species no. 2 [2.940, 93%, 1.110, 5.000 (2.0058), 13.230 (1, 1), 1.890 (0.5, 2)]. The ^{1}H-splitting for the diradical was not included. The line widths, g-shifts, and hyperfine splittings are reported in Gauss. Green trace: numerical fit for species no. 1 in isolation with above optimized parameters. (Using DPPH standard, g = 2.0058 is obtained.)

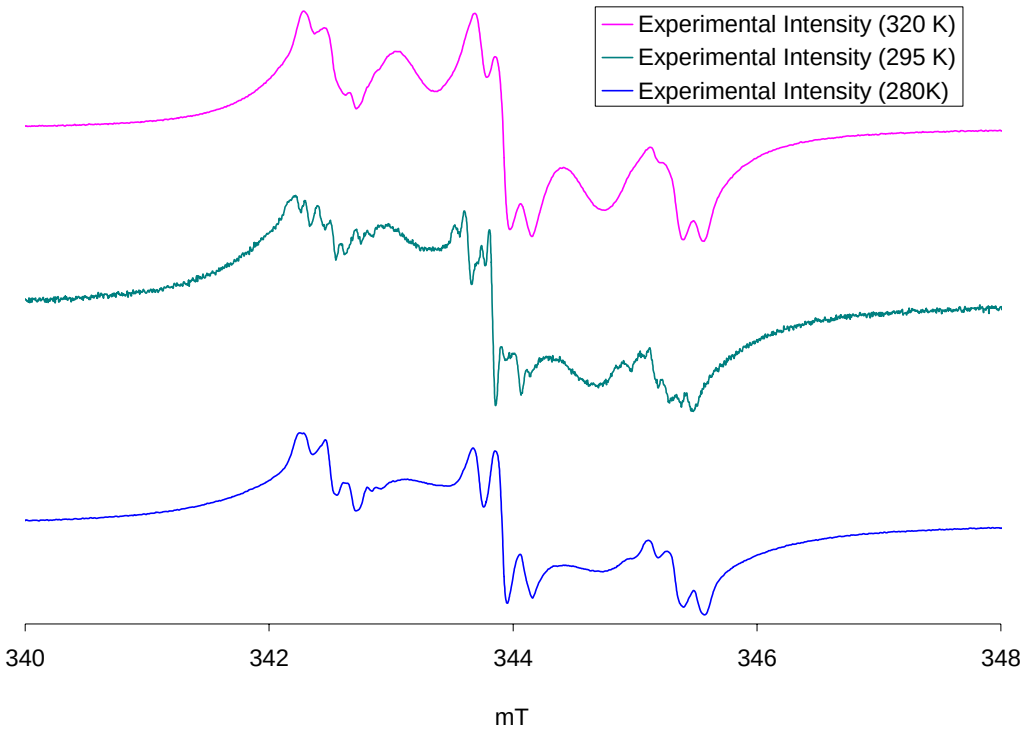

Figure S8. EPR (X-band) spectra of 1 mM nitroxide diradical **2** in DCM/MeOH (4 : 1). Purple trace (topmost): spectrum at 320 K (KS765r6). Green trace (center): spectrum at 295 K (KS1263r5). Blue trace (lowermost): spectrum at 280 K (KS765r4). Identical sample was used for spectra at 280 K and 320 K.

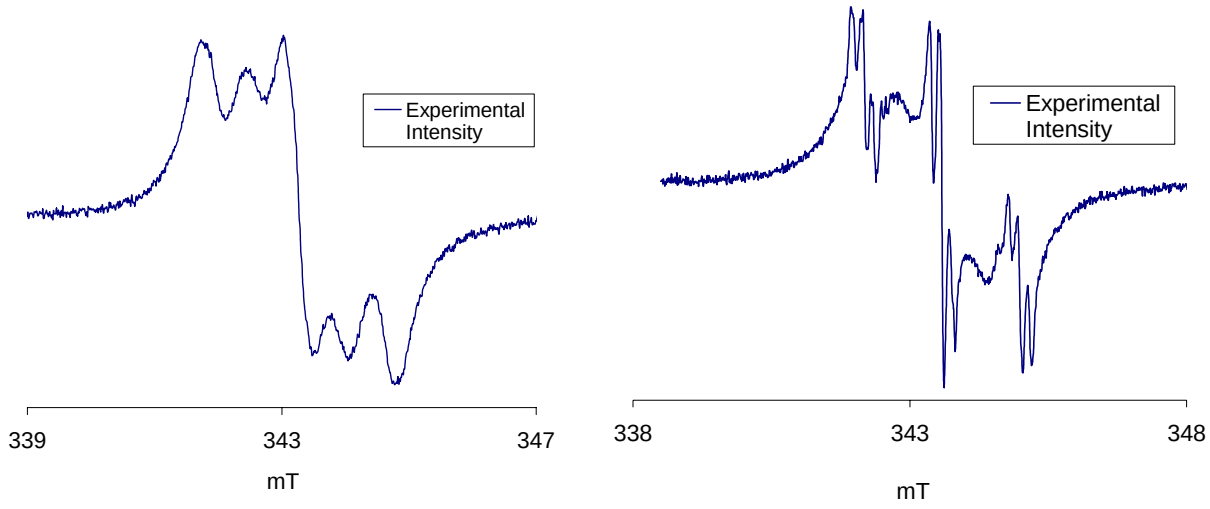

Figure S9. EPR (X-band) spectra of 1 mM nitroxide diradical **2** at room temperature. Left spectrum: **2** in acetonitrile (KS955r2). Right spectrum: **2** in dichloromethane at 297 K (KS970r2).

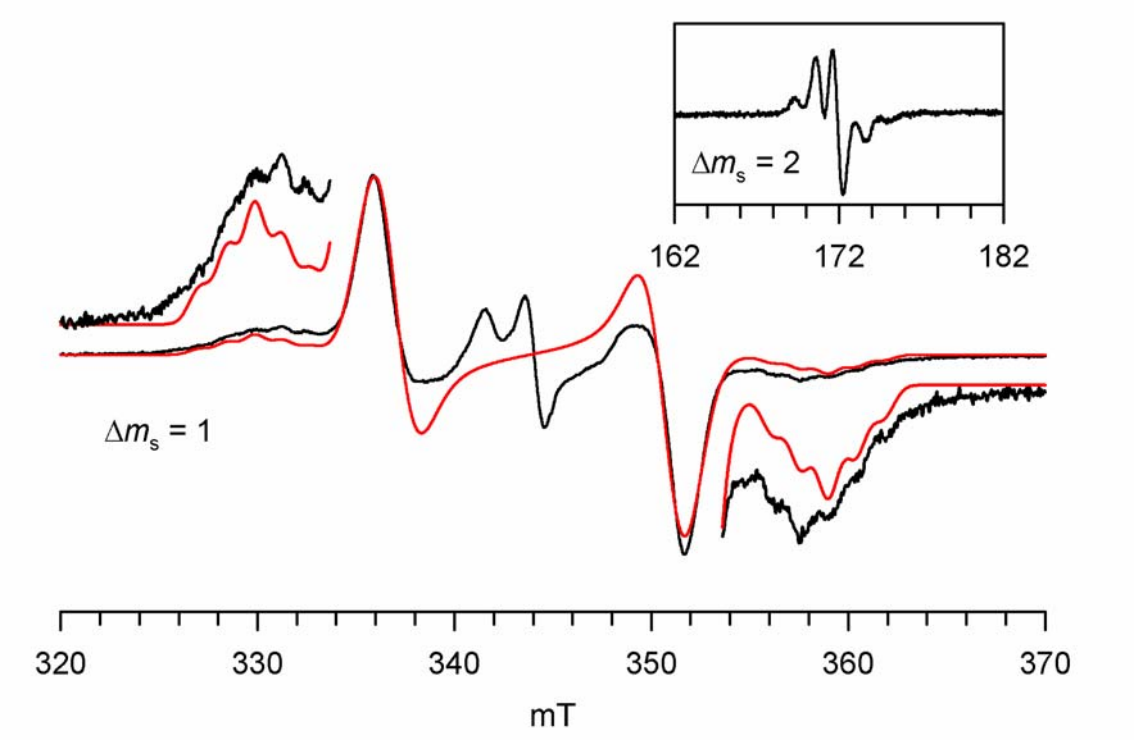

Figure S10. EPR (X-Band, 9.6561 GHz) spectrum of 1 mM nitroxide diradical **2** in dichloromethane/methanol (4 : 1) at 140 K (label: KS1263r14). The spectral simulation of the $|\Delta m_s| = 1$ region is shown as red trace. The fitting parameters for the spectral simulation for the $S = 1$ state are: $|D/hc| = 1.36 \times 10^{-2}$ cm^{-1} ($D = 145$ G), $|E/hc| = 0$ cm^{-1}, $g_x = 2.0062$, $g_y = 2.0062$, $g_z = 2.0035$, $|A_{zz}/2|/hc \approx 1.3 \times 10^{-3}$ cm^{-1}, Gaussian line ($L_x = 20$ G, $L_y = 22$ G, $L_z = 12$ G). The center lines correspond to an $S = ½$ (monoradical) impurity.

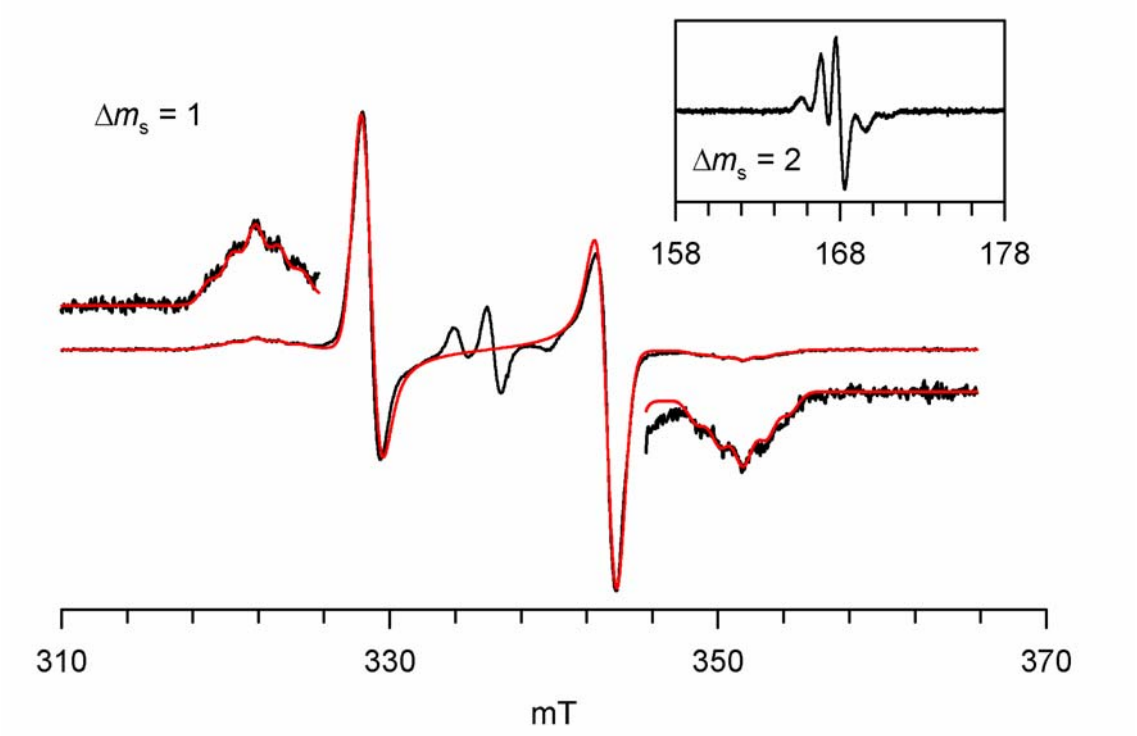

Figure S11A. EPR (X-Band, 9.4389 GHz) spectrum of 0.7 mM nitroxide diradical **2** in 2-MeTHF at 140 K (label: PT363r2/r4). The spectral simulation of the $|\Delta m_s| = 1$ region is shown as red trace. The fitting parameters for the spectral simulation for the $S = 1$ state are: $|D/hc| = 1.39 \times 10^{-2}$ cm^{-1} ($D = 149$ G), $|E/hc| = 0$ cm^{-1}, $g_x = 2.0064$, $g_y = 2.0064$, $g_z = 2.0031$, $|A_{zz}/2|/hc \approx 1.3 \times 10^{-3}$ cm^{-1}, and Gaussian line ($L_x = 11$ G, $L_y = 13$ G, $L_z = 11$ G). The center lines correspond to an $S = ½$ (monoradical) impurity.

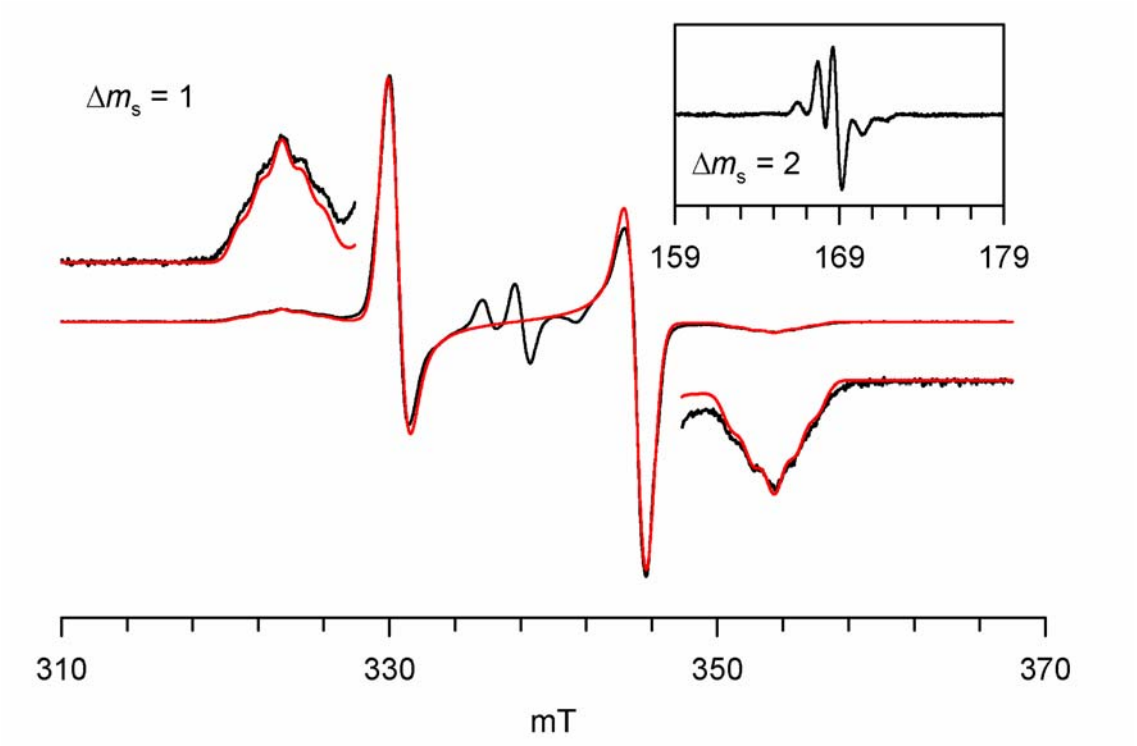

Figure S11B. EPR (X-Band, 9.4876 GHz) spectrum of 0.7 mM nitroxide diradical **2** in 2-MeTHF at 135 K (label: SM1112r4/r5). The spectral simulation of the $|\Delta m_s| = 1$ region is shown as red trace. The fitting parameters for the spectral simulation for the $S = 1$ state are: $|D/hc| = 1.405 \times 10^{-2}$ cm^{-1}, $|E/hc| = 0$ cm^{-1}, $g_x = 2.0063$, $g_y = 2.0063$, $g_z = 2.0028$, $|A_{zz}/2|/hc \approx 1.2 \times 10^{-3}$ cm^{-1}, and Gaussian line ($L_x = 11$ G, $L_y = 13$ G, $L_z = 11$ G). The center lines correspond to an $S = ½$ (monoradical) impurity.

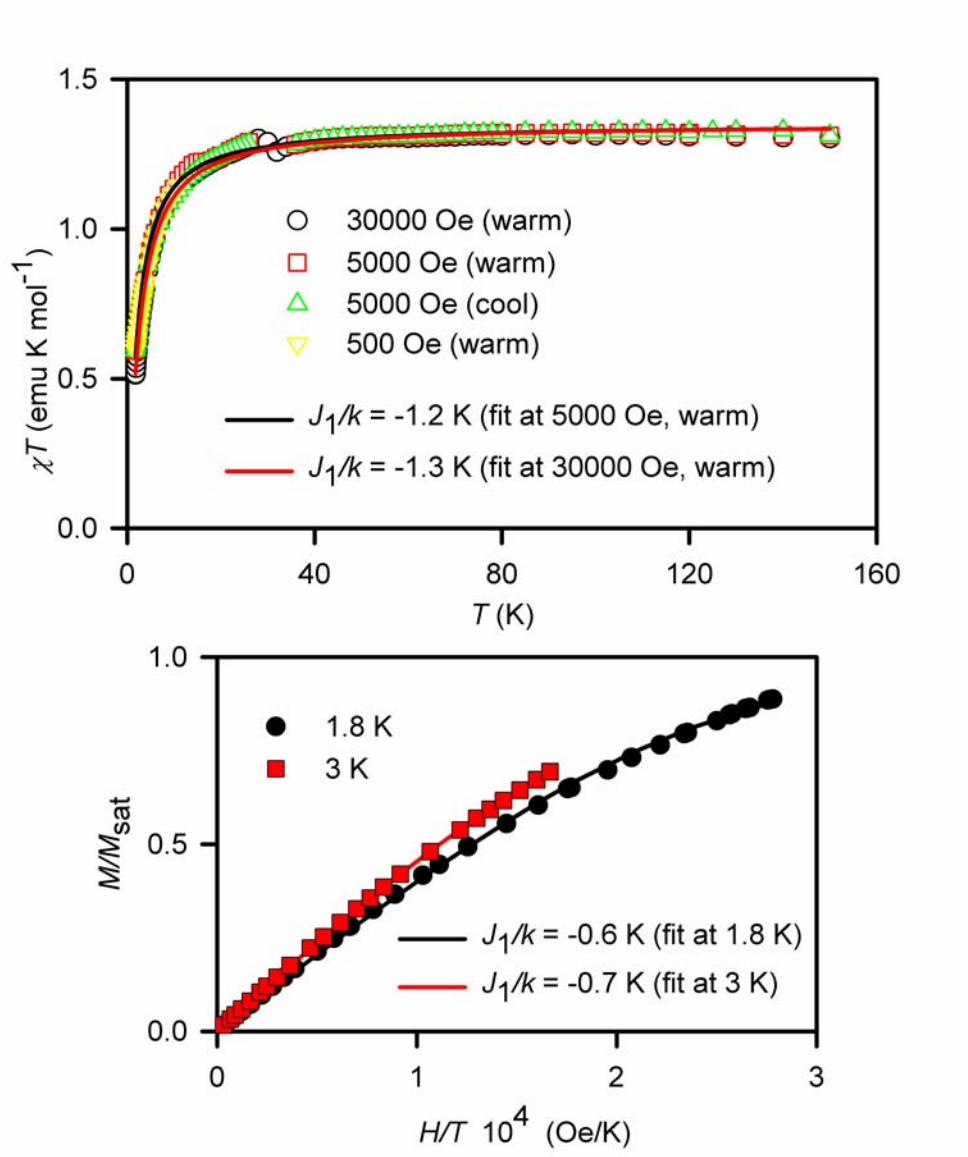

Figure S12. SQUID magnetometry for concentrated (13 mM) solution of **1** in THF (label: SM988r1F) with numerical fits to the tetraradical model (Figure 10, eq. 1 and 2). For the χT vs. T fits (top) and the M/M_{sat} vs. H/T fits (bottom), the J_2/k (diagonal coupling) is set to –1.1 K and –0.6 K, respectively. The variable parameters (parameter dependence and R^2) are as follows: at 30000 Oe in the warming mode, J_1/k = –1.3 K, w = 0.90 (0.32, 0.998); at 5000 Oe in the warming mode, J_1/k = –1.2 K, w = 0.90 (0.30, 0.995); at 1.8 K, J_1/k = –0.6 K, M_{sat} = 0.62 μ_B (0.86, 0.999); at 3 K, J_1/k = –0.7 K, M_{sat} = 0.70 μ_B (0.97, 1.000).

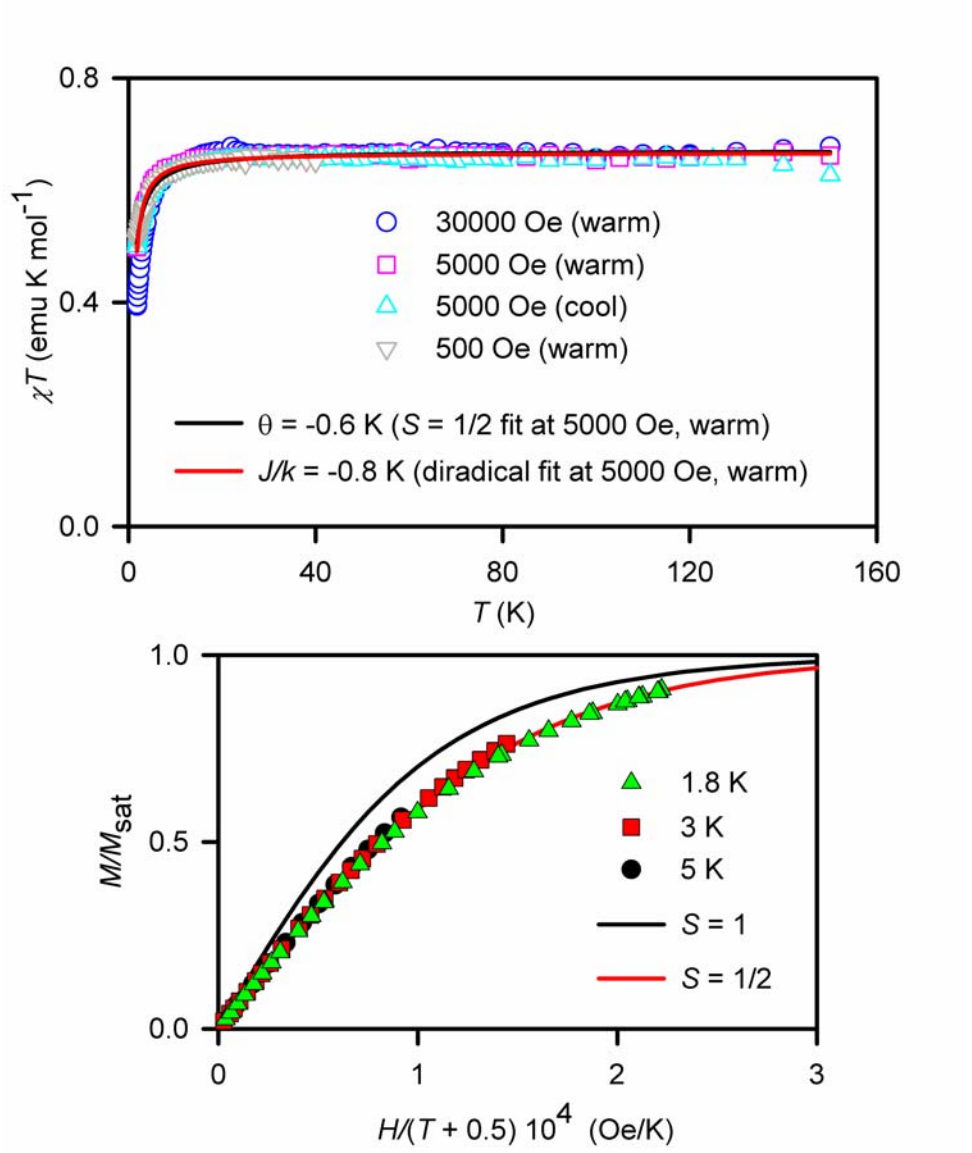

Figure S13. SQUID magnetometry for dilute (7 mM) solution of nitroxide diradical **2** in THF (label: KD1256F). The experimental data are identical to that in Figure 9 (main text). The mean-field numerical fits (θ = –0.5 K or θ = –0.6 K) are shown. For the χT vs. T data, numerical fit to the diradical model is shown for reference. In the magnetization plot, the solid lines correspond to Brillouin functions with $S = ½$ and $S = 1$.

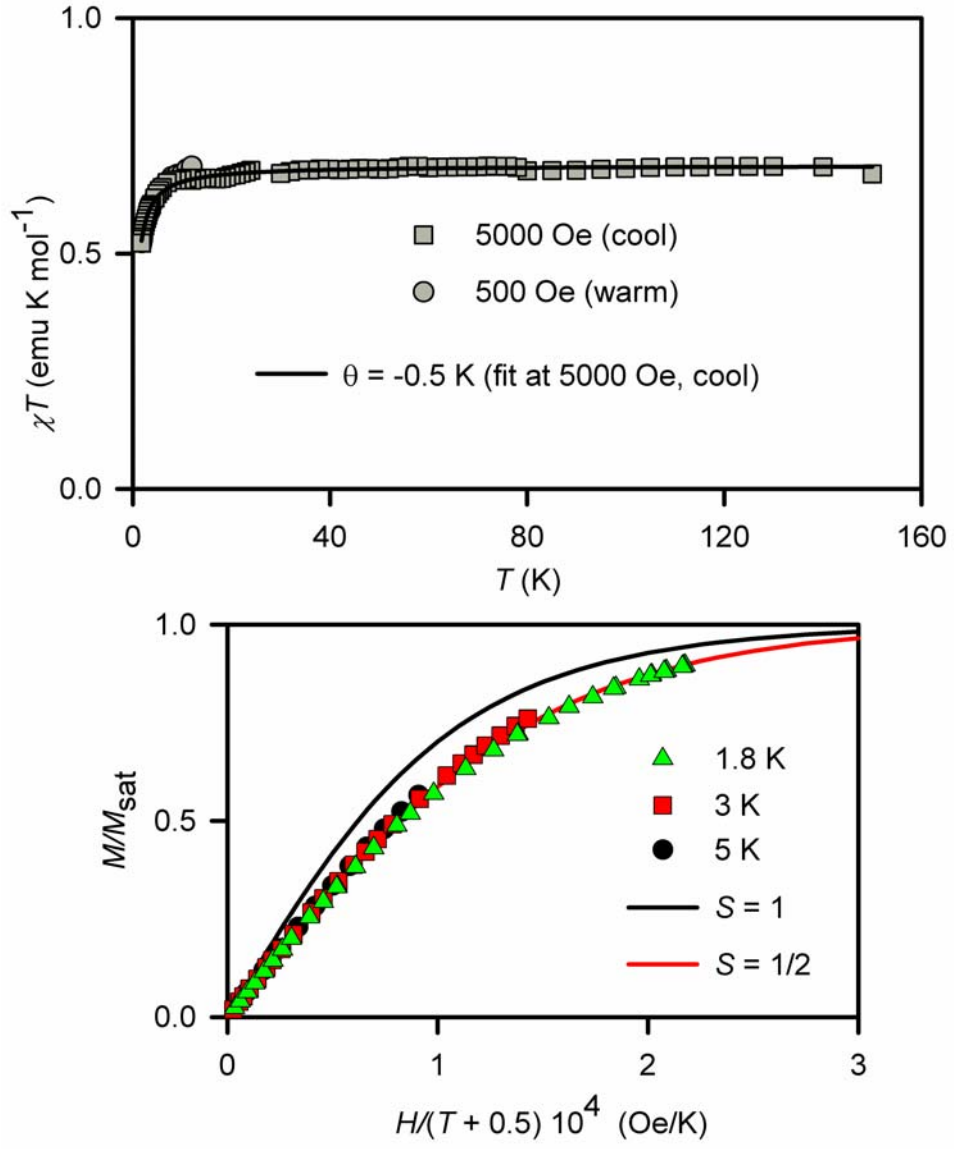

Figure S14. SQUID magnetometry for concentrated (24 mM) solution of nitroxide diradical **2** in THF (label: KD1247G). In the χT vs. T plots, the solid line corresponds to numerical fit to the Brillouin function of two independent spins $S = ½$ with the following variable parameters (parameter dependence and R^2): mean-field parameter, $\theta = –0.5$ K, and weight factor, $w = 0.91$ (0.35 and $R^2 = 0.999$). In the M/M_{sat} vs. $H/(T – \theta)$ plots at 1.8, 3, and 5 K, where $\theta = –0.5$ K is the mean-field parameter, the solid lines correspond to Brillouin functions with $S = ½$ and $S = 1$.

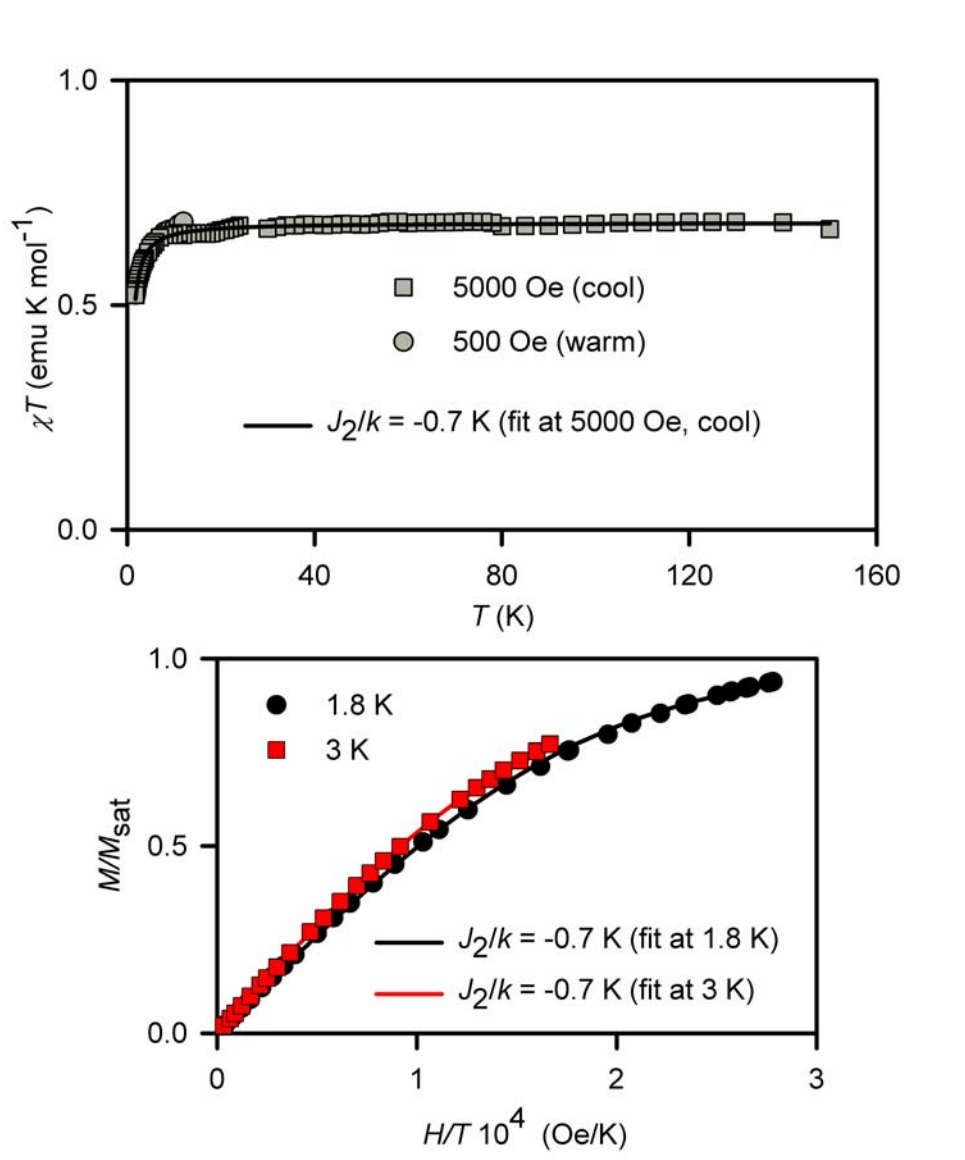

Figure S15. SQUID magnetometry for concentrated (24 mM) solution of nitroxide diradical **2** in THF (label: KD1247H) with numerical fits to the diradical model (eq. 4 with $J_1/k = 0$). The experimental data are identical to that in Figure S14. For the χT vs. T fits (top) and the M/M_{sat} vs. H/T fits (bottom), the variable parameters (parameter dependence and R^2) are as follows: at 5000 Oe in the cooling mode, $J_2/k = -0.7$ K, $w = 0.91$ (0.26, 0.990); at 1.8 K, $J_2/k = -0.7$ K, $M_{sat} = 0.85$ μ_B (0.63, 1.000); at 3 K, $J_2/k = -0.7$ K, $M_{sat} = 0.88$ μ_B (0.92, 1.000).

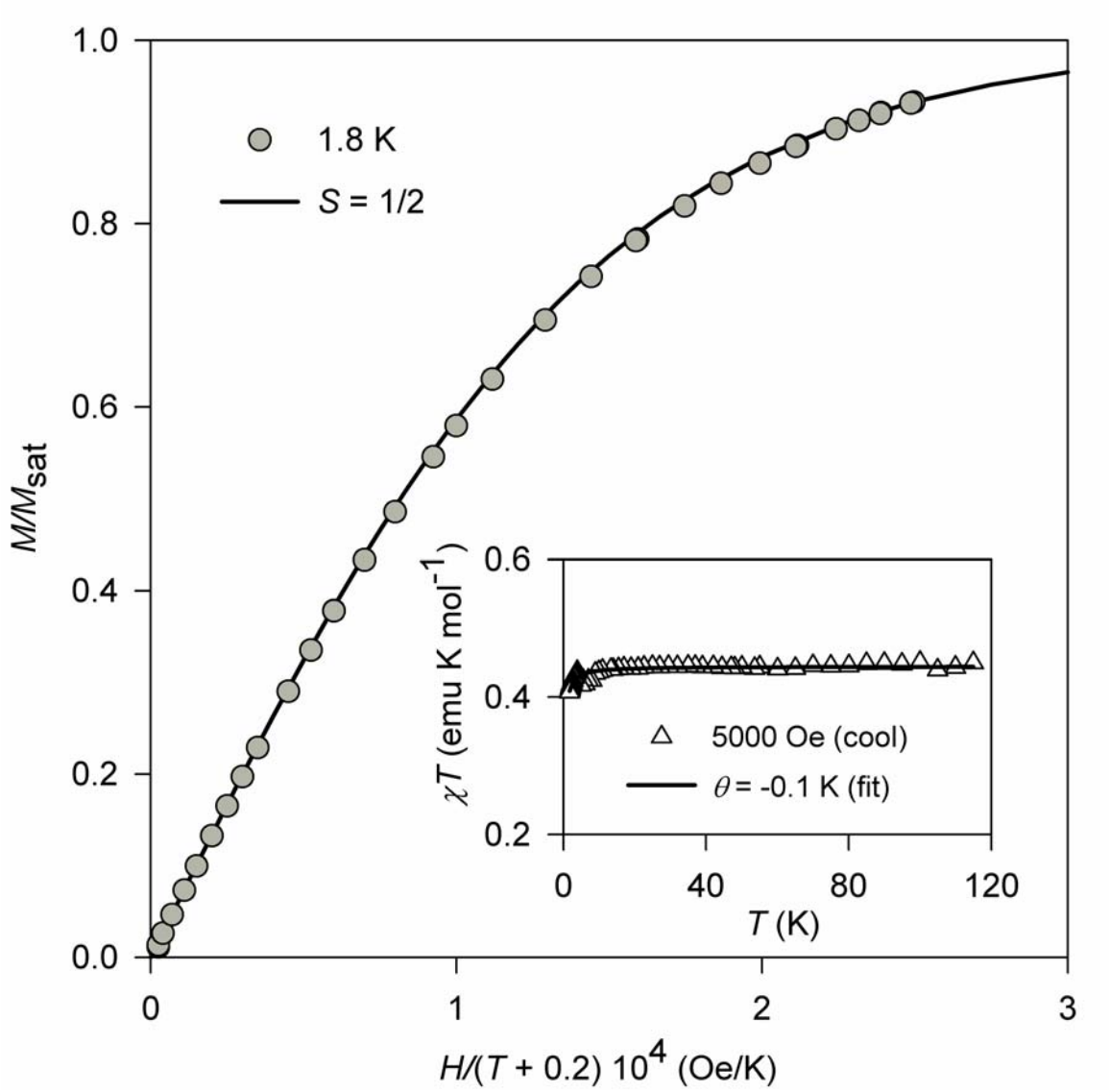

Figure S16. SQUID magnetometry for ~5 mM nitroxide diradical **2** in chloroform/methanol (1:1) (label: H0235r1G). Main plot: M/M_{sat} vs. $H/(T - \theta)$ at 1.8 K, where θ = –0.2 K is the mean-field parameter; the solid line corresponds to Brillouin function with S = ½. Inset plot: χT vs. T in cooling mode; the solid line corresponds to Brillouin function with S = ½ and mean-field parameter θ = –0.1 K.

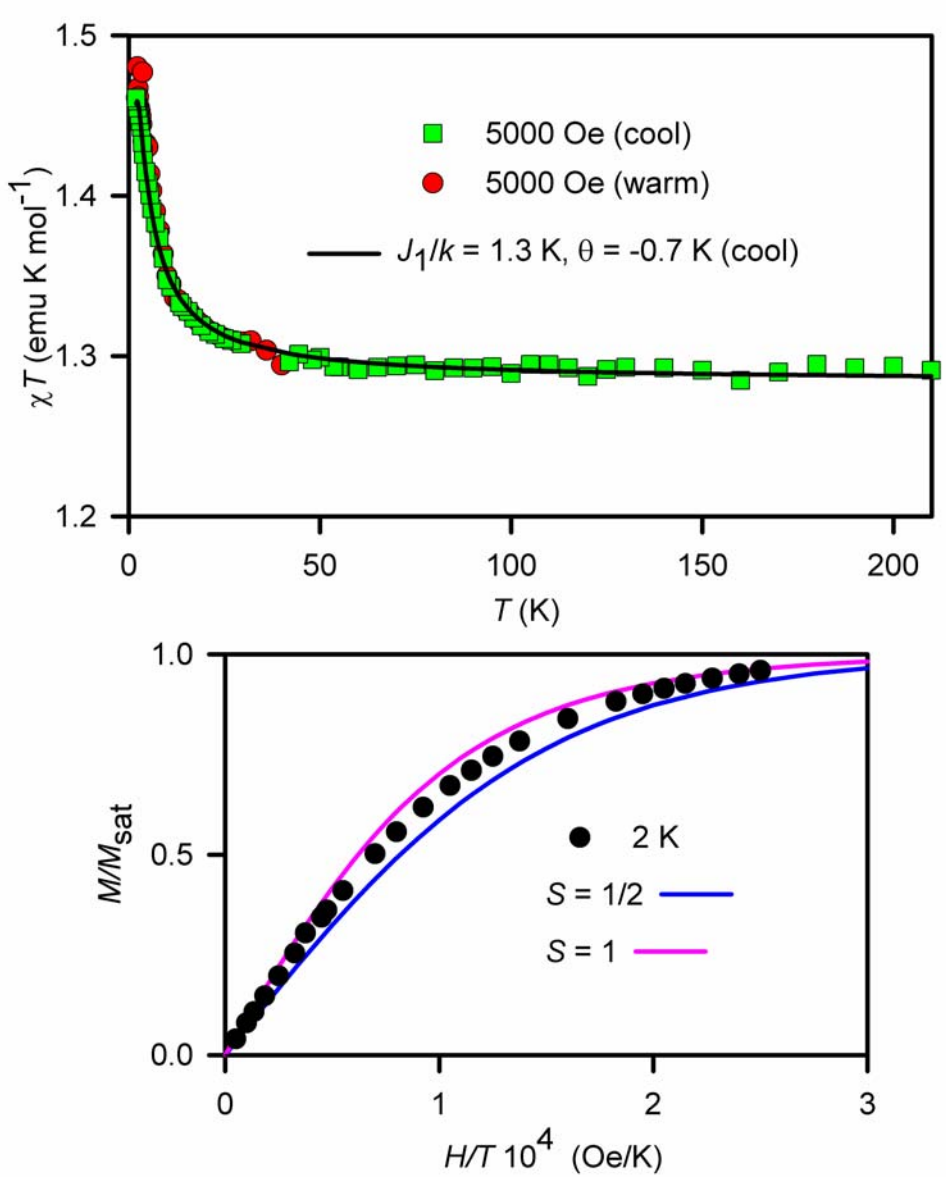

Figure S17. SQUID magnetometry for 20 mM **3** in 2-MeTHF (label: J1829RI) with numerical fit to the tetraradical model with mean-field parameter (Figure 10). The experimental data are identical to that in Figure 11 (main text). For the χT vs. T plot (top), the variable parameters (parameter dependence) for numerical at 5000 Oe in the warming mode are as follows: J_1/k = +1.3 K (0.98), θ = –0.7 K (0.98), w = 0.85 (0.56); R^2 = 0.997. For the M/M_{sat} vs. H/T plot at T = 2 K (bottom), theoretical Brillouin curves for paramagnet with S = ½ and S = 1 are shown.

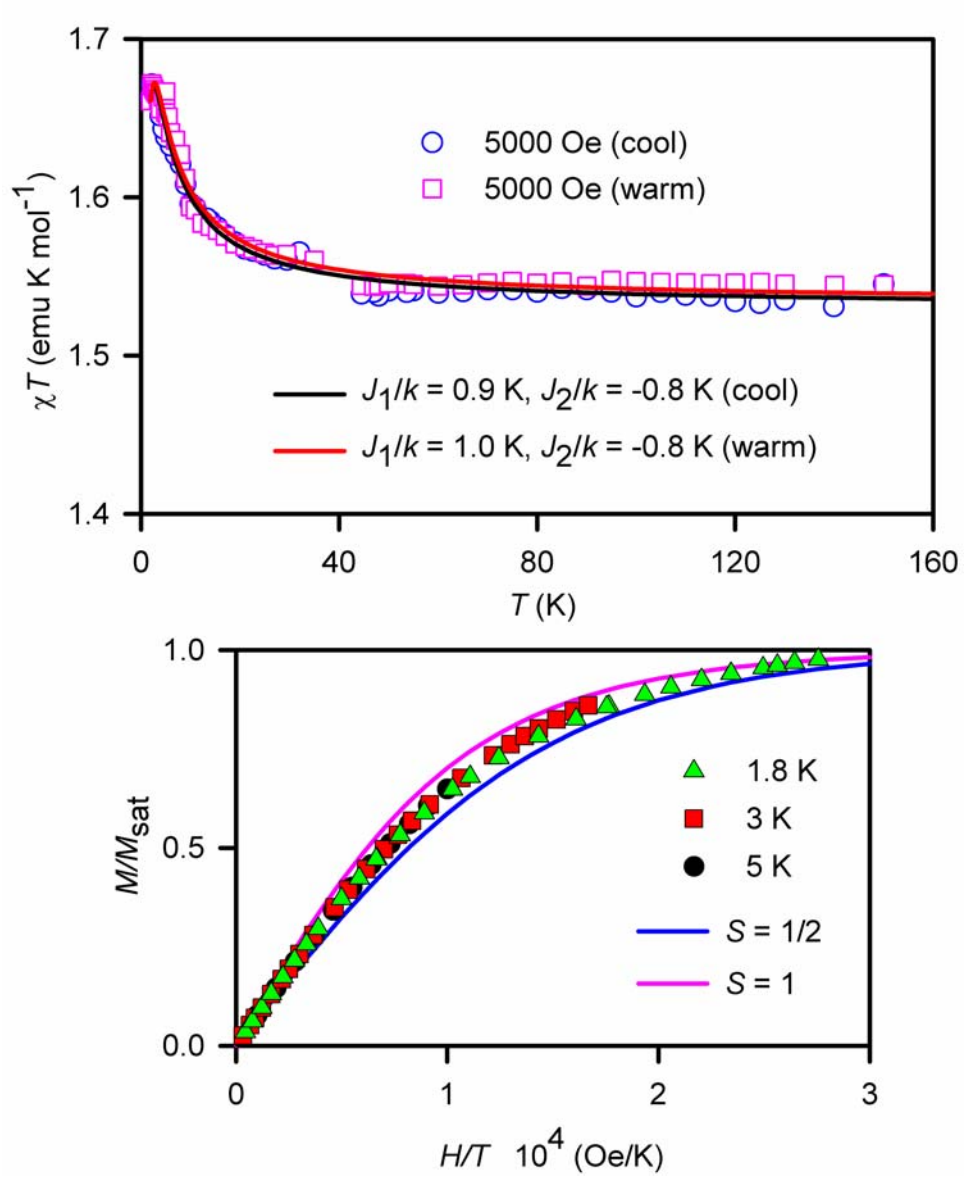

Figure S18. SQUID magnetometry for 15 mM **3** in THF (label: TR4081F3) with numerical fit to the tetraradical model (Figure 10, equation 2). For the χT vs. T plot (top), the variable parameters (parameter dependence) for the numerical fit to tetraradical model at 5000 Oe in the cooling mode are as follows: J_1/k = +0.9 K (0.98), J_2/k = –0.8 K (0.98), w = 1.02 (0.64); R^2 = 0.991. Analogous fit is obtained at 5000 Oe in the warming mode (R^2 = 0.986). For the M/M_{sat} vs. H/T plot at T = 2 K (bottom), theoretical Brillouin curves for paramagnet with S = ½ and S = 1 are shown.

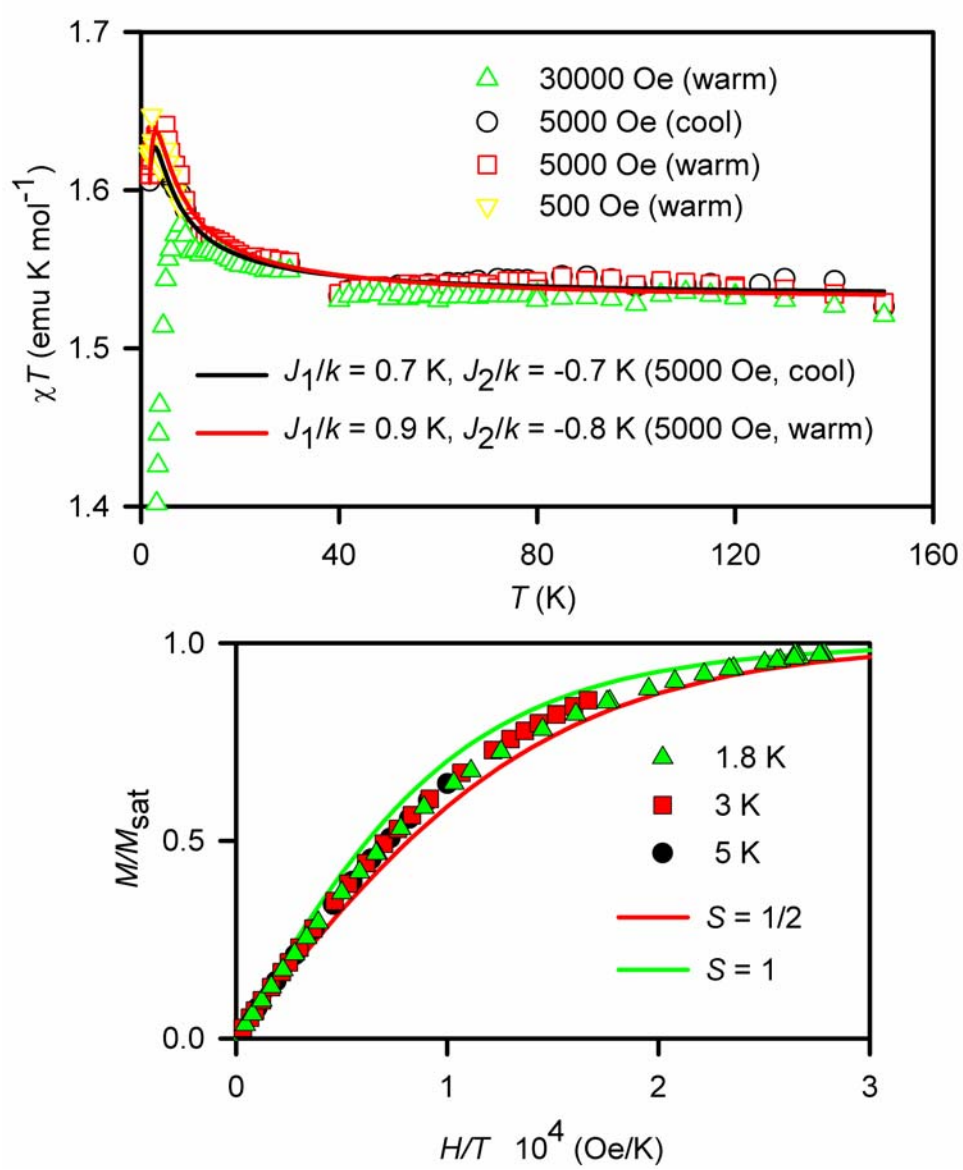

Figure S19. SQUID magnetometry for 15 mM **3** in THF (label: TR4081F6) with numerical fit to the tetraradical model (Figure 10, equation 2). For the χT vs. T plot (top), the variable parameters (parameter dependence) for the numerical fit to tetraradical model at 5000 Oe in the cooling mode are as follows: J_1/k = +0.7 K (0.98), J_2/k = –0.7 K (0.98), w = 1.02 (0.63); R^2 = 0.983. Analogous fit is obtained at 5000 Oe in the warming mode (R^2 = 0.978). For the M/M_{sat} vs. H/T plot at T = 2 K (bottom), theoretical Brillouin curves for paramagnet with S = ½ and S = 1 are shown.

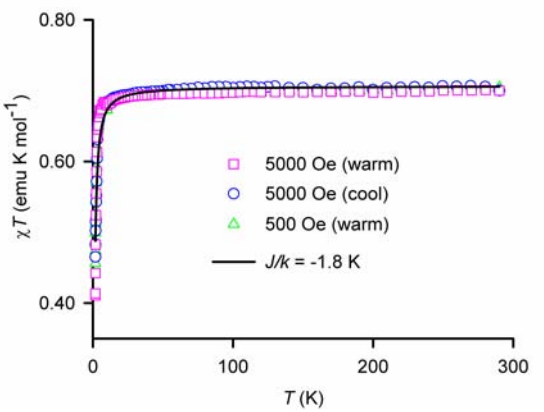

Figure S20. SQUID magnetometry for solid dinitroxide **2**: χT vs. T plots (label: H157R2H). The numerical fit (solid line) to the model of "diradical plus two S = ½ monoradicals" (eq. S5b) has the following variable parameters (and their parameter dependence) at 5000 Oe in the warming mode: J/k = –1.8 K and w = 0.94 (0.23).

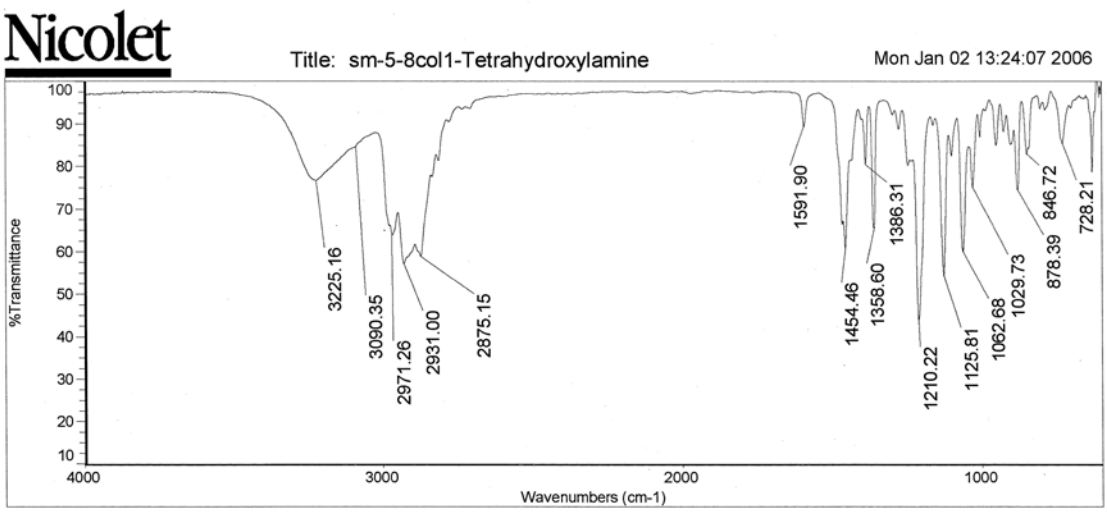

Number of sample scans: 128
Number of background scans: 128
Resolution: 4.000
Sample gain: 8.0
Mirror velocity: 0.6329
Aperture: 100.00

Figure S21. IR (ATR, ZnSe) spectrum of the calix[4]arene tetrahydroxylamine **5**.

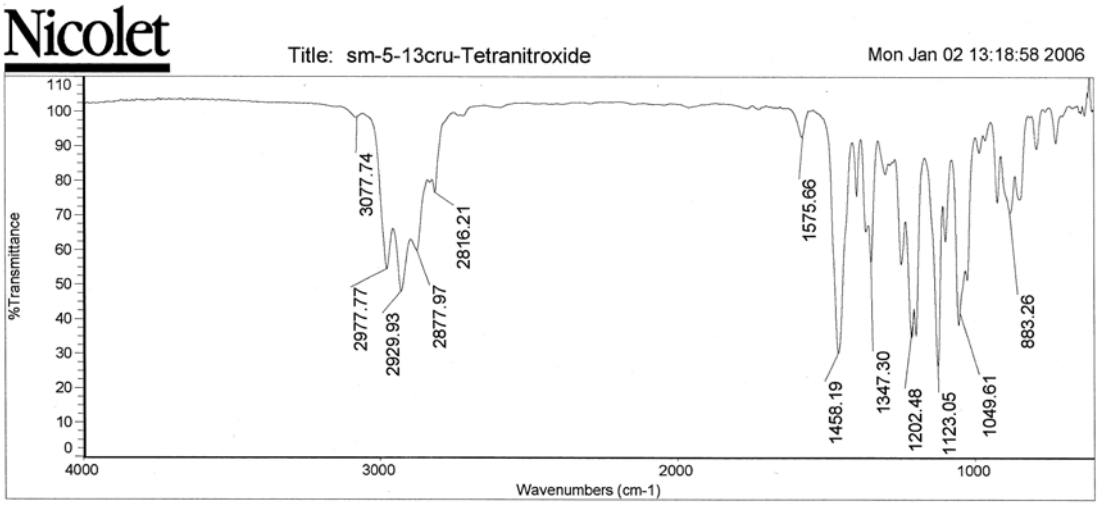

Number of sample scans: 128
Number of background scans: 128
Resolution: 4.000
Sample gain: 8.0
Mirror velocity: 0.6329
Aperture: 100.00

Figure S22. IR (ATR, ZnSe) spectrum of the calix[4]arene nitroxide tetraradical **1**.

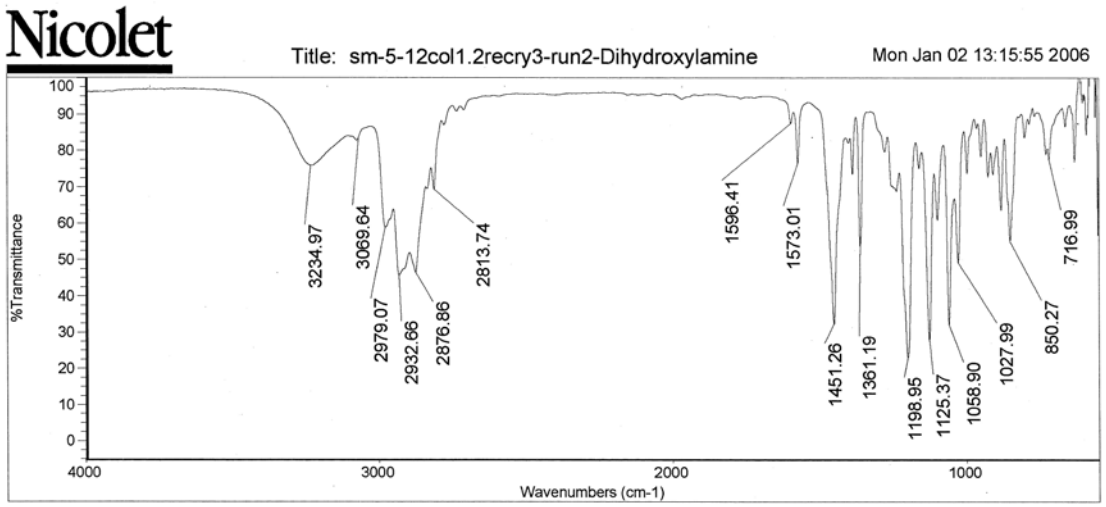

Figure S23. IR (ATR, ZnSe) spectrum of the calix[4]arene dihydroxylamine **6**.

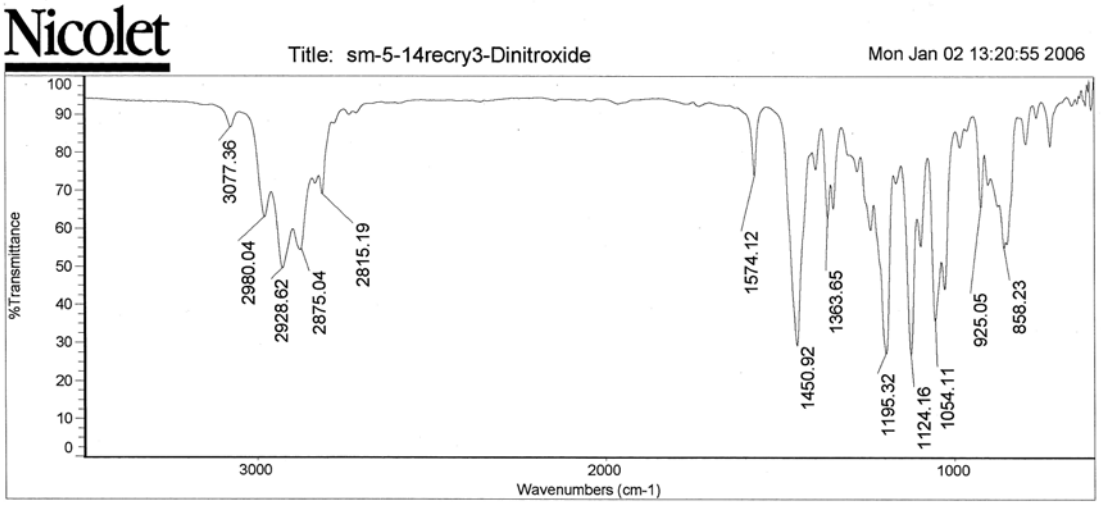

Figure S24. IR (ATR, ZnSe) spectrum of the calix[4]arene nitroxide diradical **2**.

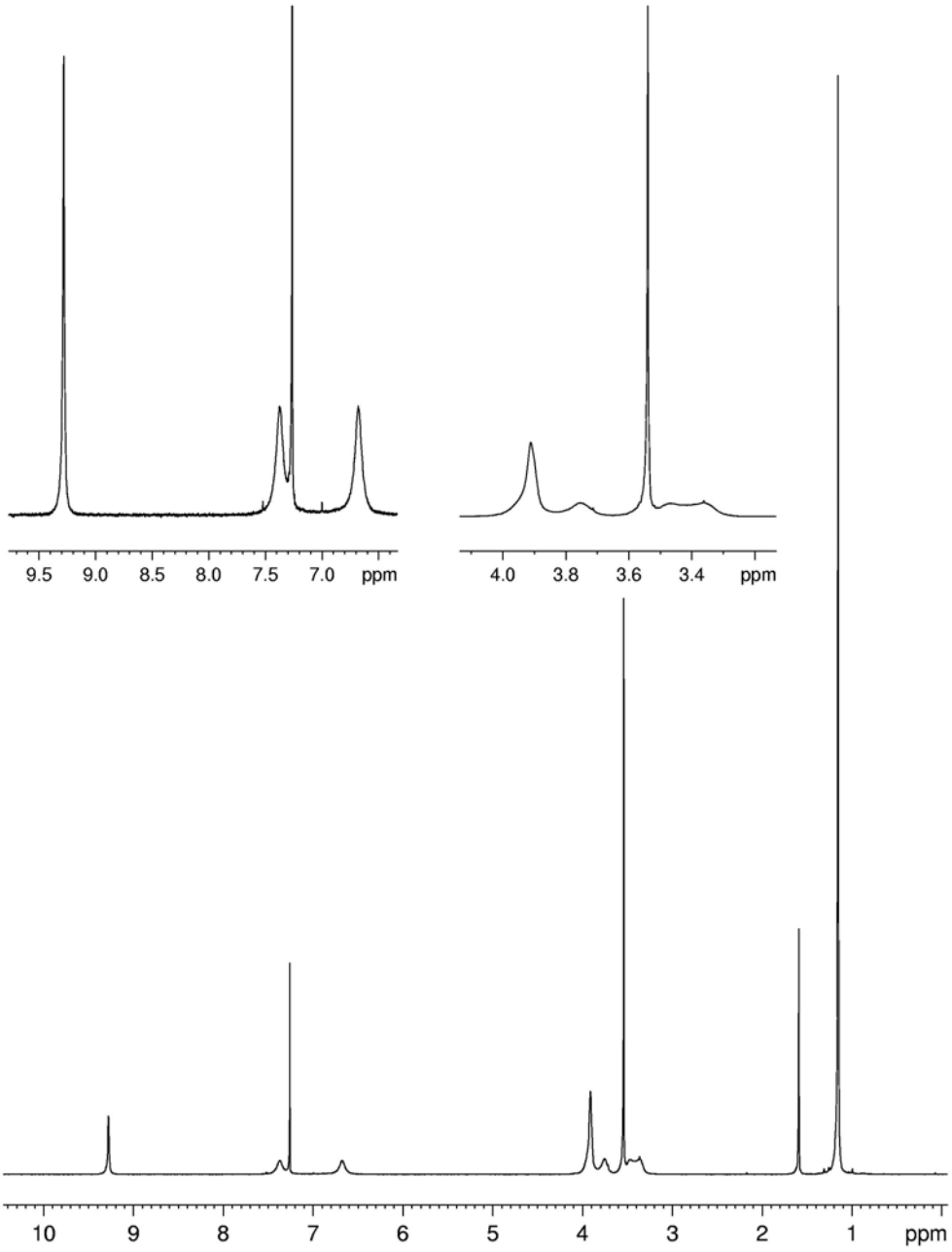

Figure S25. ^{1}H NMR (400 MHz, chloroform-*d*) spectrum of tetrahydroxylamine **5** (label: sm-10-17col1_run2).

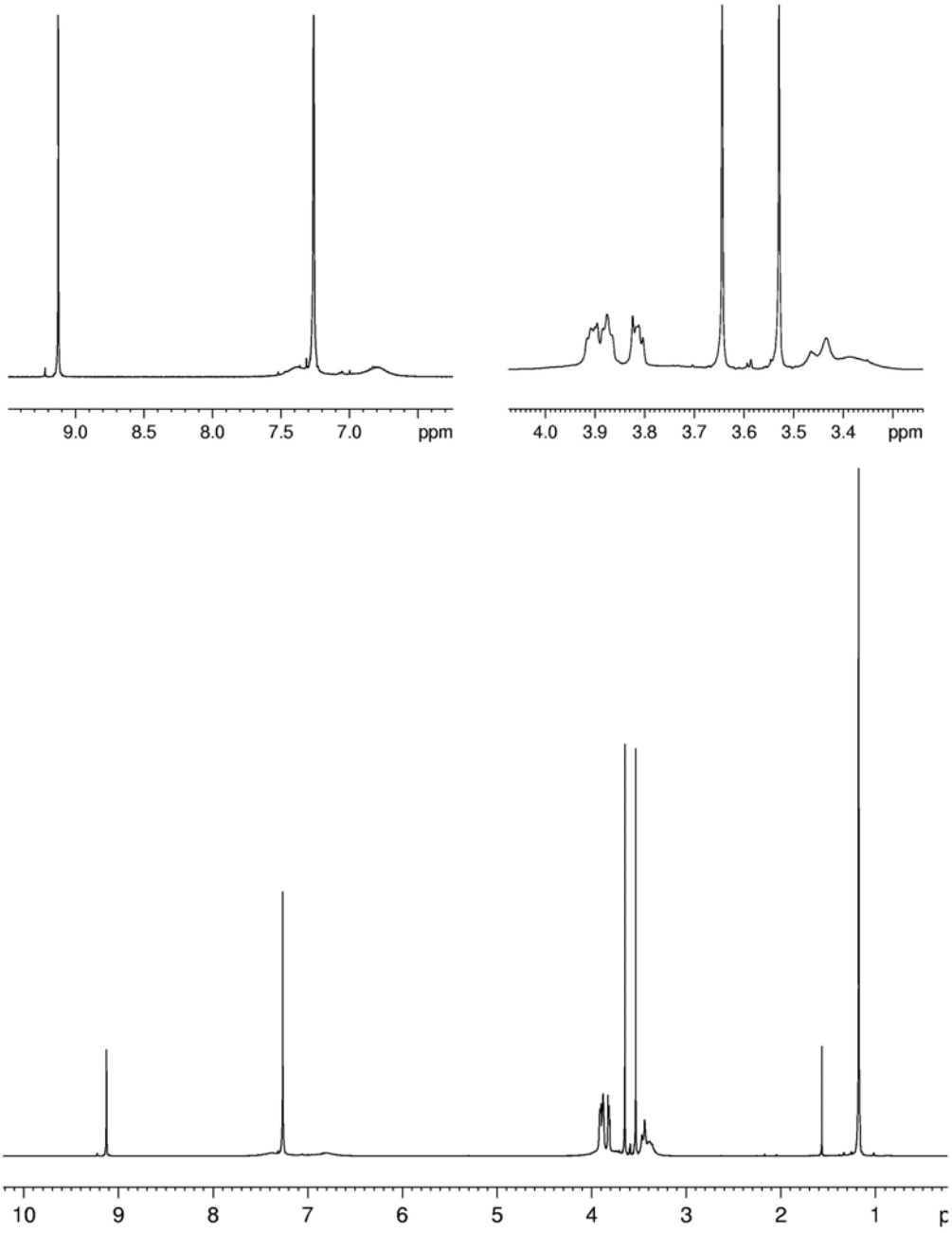

Figure S26. ^{1}H NMR (400 MHz, chloroform-*d*) spectrum of dihydroxylamine **6** (label: sm-10-11col1-run2).

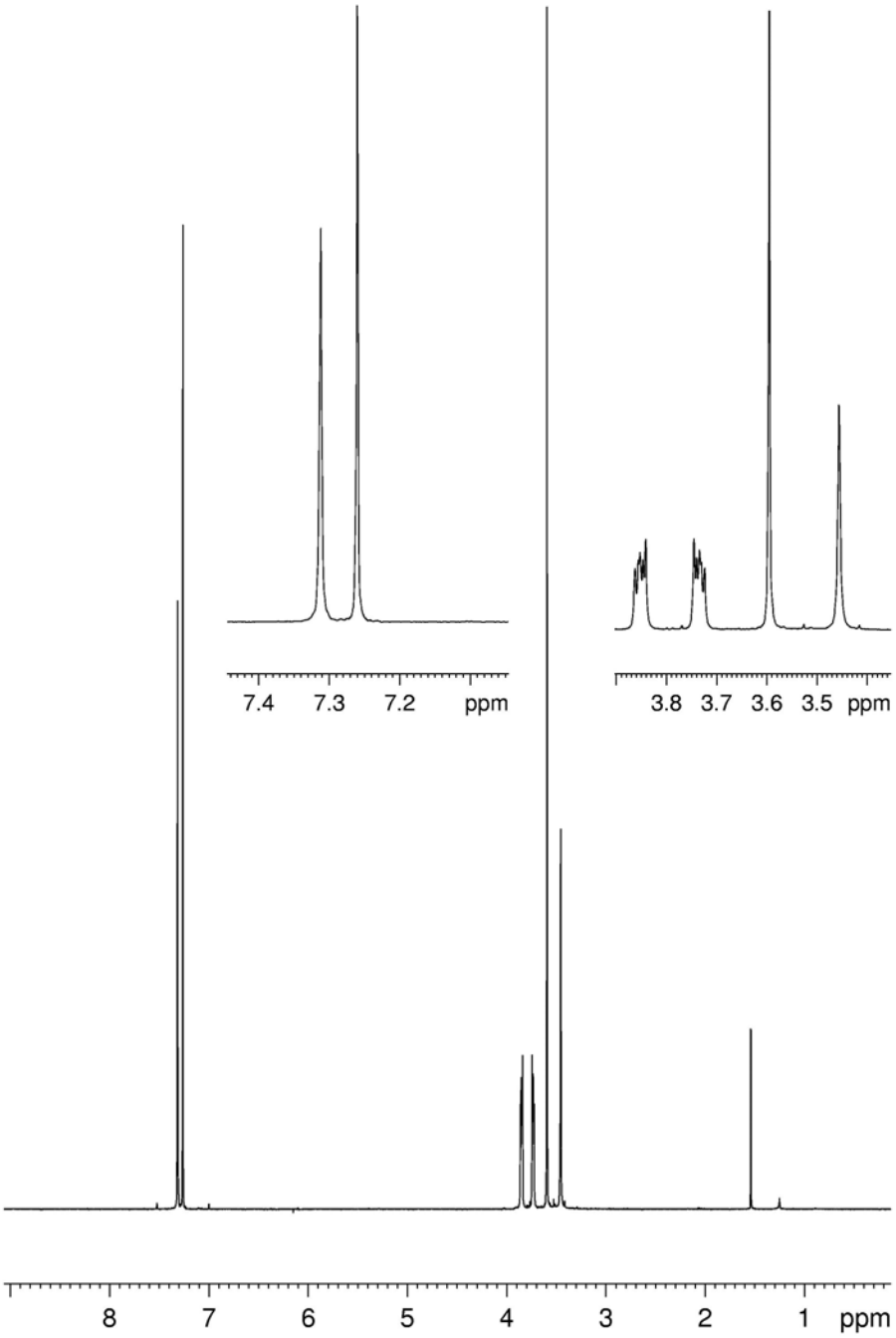

Figure S27. ^{1}H NMR (400 MHz, chloroform-*d*) spectrum of tetrabromocalix[4]arene **4** (label: SM-6-60recry1).